The GNSS Reflectometry Response to the Ocean Surface Winds and Waves

Seubson Soisuvarn, *Member, IEEE,* Zorana Jelenak, *Member, IEEE*, Faozi Said, *Member, IEEE,*

Paul S. Chang, *Member, IEEE* and Alejandro Egido, *Member, IEEE*

***Abstract*— This paper investigates Global Navigation Satellite System Reflectometry (GNSS-R) measurements collected by the Space GNSS Receiver-Remote Sensing Instrument (SGR-ReSI) on board the TechDemoSat-1 (TDS-1) satellite. The sensitivity of the SGR-ReSI measurements to the ocean surface winds and waves are characterized. The correlation with sea surface temperature (SST), wind direction, and rain are also investigated. The SGR-ReSI measurements exhibit clear sensitivity to wind speeds up to 20 m/s. There is also apparent sensitivity to 35 m/s wind speeds although the collocation dataset becomes sparser. A dependence on the swell is also observed for winds < 6 m/s. Additionally, a small correlation with SST is observed in which the slope of the SGR-ReSI measurements is positive for winds < 5 m/s, and reverses for winds > 5 m/s. A weak wind direction signal was also observed, and an investigation of rain impacts did not conclusively confirm any influence on the data. These results are shown through an analysis of global statistics as well as an analysis of several case studies. This publicly released SGR-ReSI dataset provided a first opportunity to comprehensively investigate the sensitivity of GNSS-R measurements to various ocean surface parameters. The upcoming NASA Cyclone Global Navigation Satellite System (CYGNSS) will utilize a similar receiver to the SGI-ReSI, therefore, this data provides valuable pre-launch insight.**

***Index Terms*—GNSS-R, CYGNSS, Scatterometry, Ocean Surface Winds**

The authors are with the Center for Satellite Applications and Research (STAR), NOAA/NESDIS, 5830 University Research Ct., College Park, MD 20740 USA (e-mail: seubson.soisuvarn@noaa.gov).

I. Introduction

GLOBAL Navigation Satellite System – Reflectometry (GNSS-R) exploits signals of opportunity from the Global Navigation Satellite System (GNSS). GNSS transmitters continuously transmit navigation signals at L-band toward Earth's surface. The scattered power reflected off Earth's surface can be sensed by specially designed GNSS-R receivers. The reflected signal can be used to glean information about Earth's surface such as ocean surface roughness, snow depth, sea ice extent, and soil moisture. The use of GNSS-R for ocean wind retrievals was first demonstrated from aircraft [1]. Zavorotny *et.al.* [2] provide a theoretical model which shows that the scattered power of a GPS signal depends on the probability density function of surface slopes that are contingent upon local wind conditions. Garrison *et. al.* [1] demonstrated the use of GNSS-R for ocean wind retrievals using measurements from an aircraft GNSS-R receiver. Data was collected by the first spaceborne GNSS-R receiver on the United Kingdom- Disaster Monitoring Constellation (UK-DMC), an Earth observation satellite launched by Surrey Satellite Technology, Ltd in 2003. UK-DMC's dataset also exhibited the ocean wind and wave sensing potential of the GNSS-R technique [3], [4]. While the UK-DMC dataset did demonstrate wind and wave dependence in the GNSS-R signal, the approximately 40 data points were too limited to fully characterize the ocean wind retrieval capabilities of GNSS-R from space.

On July 8, 2014, the TechDemoSat-1 satellite (TDS-1) was launched by Surrey Satellite Technology, Ltd. as a technology risk reduction mission into a sun-synchronous orbit. One of the payloads carried on board the TDS-1 is the Space GNSS Receiver-Remote Sensing Instrument (SGR-ReSI). With its specially designed nadir pointing antenna and associated antenna pattern (see Fig. 1), the SGR-ReSI is capable of retrieving 4 Delay Doppler Maps

(DDMs) simultaneously (see [5] for additional instrument specifications). The upcoming NASA Cyclone Navigation Satellite System (CYGNSS) mission will utilize similar GNSS-R receivers [6].

TDS-1 has already provided significantly more DDM measurements over the ocean than previously collected. A thorough analysis of the dependence of these DDM measurements to various ocean surface conditions, such as the mean square slope (MSS), wind speed, significant wave height, sea surface temperature, and wind direction are presented and discussed in this paper. The potential rain impact on GNSS-R measurements is also discussed.

TDS-1 SGR-ReSI data are made available to the user community through the Measurement of Earth-Reflected Radio-navigation Signals By Satellite (MERRByS) website at http://www.merrbys.co.uk. The publicly released SGR-ReSI dataset used in this paper is version 0.3. The data products consist of raw collections of digitized intermediate frequency samples (Level 0), reflections processed into DDMs (Level 1), and derived geophysical parameters (Level 2) [7]. The current dataset available for download covers several days between September 2014 and February 2015 (see Fig. 2).

The derived geophysical parameters provided in the Level 2 product are wind speed and mean square slope derived from the Level 1 data using a preliminary retrieval algorithm developed by the United Kingdom's National Oceanography Centre (NOC) as reported in [7]. We evaluated the Level 2 products provided in this dataset [8] and found significant errors. It was later determined that the errors in the Level 2 data products (March 2015 version) were the result of an error in the implementation of the NOC algorithm in the MERRByS ground-processor. The analysis presented in this paper utilizes Level 1 data.

II. Dataset

A. Collocation Database

To evaluate the TDS-1 SGR-ReSI observations, the Level 1 dataset was collocated with datasets from several active and passive spaceborne microwave sensors such as the Advanced SCATterometer (ASCAT) [9], the RapidScat [10], the Advanced Microwave Scanning Radiometer (AMSR2) [11], the Global Precipitation Measurement (GPM) Microwave Imager (GMI) [12], the Special Sensor Microwave Imagers (SSMI-F16 and SSMI-F17) [13], and the WindSat Polarimetric Radiometer [14]. Measurements from each sensor were spatially and temporally collocated within 25 km and 90 minutes, respectively, to the SGR-ReSI observations. The SGR-ReSI matchup collocation areas with ASCAT, RapidScat, and GMI sensors are depicted on the maps in Fig. 3. The TDS-1, ASCAT, and RapidScat orbits at the collection times were complementary as seen in (Fig. 3 a, b and c). Collocations with GMI tended to be temporally stratified by latitude with the majority of the matchups having a time difference less than 20 minutes occurring between 30-60° N and S. However, these are potentially useful for investigating rain impacts on the GNSS-R signal. Spatially, the majority of ASCAT and GMI collocations were within 15 km, and the RapidScat collocations were within 10 km (Fig. 4).

In addition to measurements from the aforementioned satellite remote sensing instruments, wind and wave parameters from several numerical models were also collocated with SGR-ReSI observations. Wind parameters from the 0.25°, global-gridded, 6-hourly forecast fields from the European Centre for Medium-Range Weather Forecasts (ECMWF) numerical weather prediction (NWP) model, and the 1°, gridded, 6-hourly reanalysis fields from National Oceanic and Atmospheric Adminstration's (NOAA) Global Data Assimilation System (GDAS)

model were interpolated in space and time to the SGR-ReSI measurment locations. Fig. 5 depicts the wind speed probability density function (PDF) of the collocated SGR-ReSI data with ASCAT, RapidScat, and GMI along with the two global model winds. While the ASCAT winds are assimilated into the ECMWF and GDAS NWP models, neither ECMWF or GDAS assimilate the same ASCAT wind product that we utilized in this study. The sea surface wave related parameters generated from both the NOAA [15] and the French Research Institute for Exploitation of the Sea (IFREMER) [16] [17] WAVEWATCH (WW) numerical models were interpolated in space and time to the SGR-ReSI measurement locations. The WW models spatial and temporal sampling is 0.50° and 3-hourly, respectively. The input wind forcing used for the NOAA and IFREMER WW models are from the GDAS and ECMWF NWP models, respectively. We note that the IFREMER WW product does not provide input winds as part of its output product. Although not shown in this paper, both WW models were found to be consistent with one another. The presented analyses and results hereafter are exclusively done using the IFREMER WW variables since it is the only model that provides the MSS variable. Finally, a 0.72 Hz cut-off frequency was used to compute the MSS [16], [18]. Comparison between the TDS-1 SGR-ReSI data and the MSS inferred from altimeter measurements may be carried out to carefully assess the impact of this cut-off frequency.

The ASCAT wind products used in our analysis are the 25 km NOAA ASCAT wind products that utilize a high wind geophysical model function for C-band scatterometers as defined in [19]. This product is different than the Royal Netherlands Meteorological Institute's ASCAT wind products that are routinely assimilated in the ECMWF and GFS NWP models. NOAA's ASCAT wind product was developed for direct utilization by NOAA's National Weather Service forecasters, and validation of NOAA's ASCAT wind product is given in [19]. RapidScat wind products produced by Jet Propulsion Laboratory (JPL) and radiometer wind products produced by Remote Sensing Systems (RSS) utilized in our collocation database are not assimilated in either of the global NWP models used. Validation of the RapidScat winds show a 0.23 m/s wind speed bias with a 1.11 m/s root mean square (rms) error,

and a 1.6° wind direction bias with a 20.4° rms error with respect to buoy data [20]. While the overall reported bias and rms for RapidScat winds are small, the International Space Station (ISS) on which the RapidScat instrument is placed is not optimal, and attitude variability introduces biases. NOAA has implemented daily monitoring routines of the RapidScat winds on http://manati.star.nesdis.noaa.gov/datasets/RSCATData.php to help track the data quality. Although the daily average wind speed bias changes might be relatively small (0.1-0.5 m/s), the uncertainty of the individual wind retrievals at higher wind speeds (> 20 m/s) can be much larger. In comparison, the ASCAT wind speed bias has remained within ~0.1 m/s with respect to both the GDAS model winds and all available radiometer winds as presented by [21]. High wind validation performed with aircraft-based Step Frequency Microwave Radiometer wind and GPS dropsondes revealed a 0.68 m/s and 0.57 m/s bias with standard deviation error of 0.77 m/s and 1.72 m/s, respectively, as presented in [19].

All radiometer wind products utilized in our analysis were obtained from Remote Sensing Systems (RSS). As a part of the Satellite Intercomparison Calibration Project (http://www.remss.com/research/climate), RSS intercalibrated all satellite microwave radiometer sensors with each other, and released an intercalibrated wind speed product [22]. The RSS wind retrieval algorithm used for all satellite radiometer data was developed using WindSat polarimetric measurements [23]. Comparison with buoys shows a -0.24 m/s bias and 0.93 m/s standard deviation error globally in rain-free conditions. High wind speed retrievals (>15 m/s) were trained utilizing the Real-time Hurricane Analysis System (HWind) analysis product provided by NOAA's Atlantic Oceanographic and Meteorological Laboratory Hurricane Research Division (HRD) over tropical cyclones [23]. High wind validation with Greenland tip-jet aircraft measurements revealed a 1.65 m/s bias and 1.21 m/s standard deviation error [24]. Relative to buoy and GDAS model winds, WindSat winds at 25 m/s are on average biased 5 m/s higher [25] while relative to the NOAA ASCAT winds they are on average 2.3 m/s higher for the same wind speed. The RapidScat model function utilized in the JPL wind retrieval algorithm was optimized to match WindSat high winds.

As discussed, the performance of the wind products from the satellite sensors utilized in this study has been previously validated by the respective mission science teams and communities. While there is general acceptance in the remote-sensing science community regarding the performance of remotely sensed wind products up to moderate wind speeds (~ 20 m/s), the wind product performance at higher wind speeds becomes more problematic; sensor spatial resolution and sensitivity to strong winds, spatial resolution of observed wind gradients, the characteristics of high wind speed data sources used for geophysical model function development and validation, and proper seperation of atmospheric and surface signals in the measured signal can all affect the higher wind speed retrieval performance. How these factors are addressed has generally been varied among the wind product developers, although there are ongoing efforts to coordinate how the community approaches the development and validation of high wind speed remote sensing products. Understanding these factors at higher wind speeds is important as we analyze the sensitivity of SGR-ReSI measurements against other wind products. While the absolute value of the high wind speeds might be open for interpretation, the important factor to observe will be the trend in measurement sensitivity.

We would like to note that all satellite wind data were quality controlled using quality flags provided by the wind product developers. Also, all winds utilized in our analysis are referenced to a 10 m height.

To explore the sensitivity of the SGR-ReSI signal to sea surface temperature variations, we utilized the NOAA 0.25°, daily Optimum Interpolation Sea Surface Temperature (OISST) in addition to the SST fields provided by the ECMWF and GDAS models. OISST is an analysis constructed by combining observations from different platforms (satellites, ships, buoys) on a regular global grid. A spatially complete SST map is produced by interpolating to fill in gaps.

B. DDM Signal-to-Noise Ratio

The released SGR-ReSI DDM dataset was collected while the receiver operated in an unmonitored Automatic Gain Control (AGC) mode. At each specular point location the DDM was processed into 20 bins in the Doppler domain and 128 bins in the delay domain. The Doppler bin size is fixed at 500 Hz, and the Doppler range spans between -5,000 Hz and 4,500 Hz. The delay range spans ~0.03 ms corresponding to approximately ±15 chips. In this mode, changes in the measurement geometry and ocean surface conditions resulted in automatic gain adjustments to maintain a nominal input signal level to the analog-to-digital converter [26]. Unfortunately, these gain adjustment values were not recorded, which made it impossible to directly relate the recorded received signal power to the ocean surface parameters. Thus, we utilized the observable, DDM signal-to-noise power ratio (SNR), as defined in equation (1)

$$DDM_{SNR} = \frac{DDM_{Power} - \langle Noise \rangle}{\langle Noise \rangle}, \tag{1}$$

where DDM_{Power} is the raw count of the signal plus noise power from the 'Zoom Transform Correlator' (ZTC) unit as defined in [26]. The $<Noise>$ in (1) is the noise power as seen at the antenna and includes the system's thermal noise (i.e., contributions from the components of the receiver). We calculated the $<Noise>$ as the average of the noise floor across the Doppler domain (20 Doppler bins) and the negative delay domain (20 chip bins) of the DDM_{Power} as shown in Fig. 6,. which is computed in dB for easier visual appearance. The negative delay bins correspond to measurements at points above Earth's surface where there are no GPS reflection signals [27]. Equation (1) largely cancels out the varying gain effects introduced by the AGC circuit because both the signal and noise experience the same varying gain. The $<Noise>$ is calculated for each DDM since it will vary from DDM to

DDM as the gain varies. The 20 by 20 delay-Doppler bins used to calculate the average noise is offset from the 0 delay line by 5 delay bins to avoid contamination from the specular point power. To confirm that the noise calculations were not contaminated from any jitter and drift of the specular point signal, we investigated the <*Noise*> sensitivities to different geophysical parameters and found no measurable dependencies. The calculation in (1) is done in physical units.

Once the DDM_{SNR} is computed, we focused on two observables: 1) the peak SNR (SNR_{PEAK}) found at the specular point (see the black dot on Fig. 6), and 2) the SNR waveform (SNR_{WAVE}) defined as the power-vs.-delay waveform along the 0 Hz Doppler line (see Fig. 6). The SNR_{PEAK} value is obtained by searching for the maximum (peak) value of the SNR_{WAVE}. Given a system resolution of 1 chip, the spatial resolution at the peak of the signal is ~ 40 – 50 km up to a 35° incidence angle.

Before discussing the sensitivity of these two parameters to geophysical parameters, let us first consider the power of the GPS signals scattered off the surface towards the receiver. As shown in [2], the mean received power as a function of the delay, τ, and Doppler, f_D, with respect to the specular point is modeled as the surface integral of the radar equation at any point on the surface, given by $\vec{\rho}$

$$\left\langle \left| Y(\tau, f_D) \right| \right\rangle = K \int_A \frac{G_{ant}(\vec{\rho}) \cdot \sigma^0(\vec{\rho}) \chi^2(\vec{\rho}; \tau, f_D)}{R_{tx}^2(\vec{\rho}) \cdot R_{rx}^2(\vec{\rho})} d\vec{\rho}\,, \tag{2}$$

where K includes transmitted signal power and GPS antenna gain, which were not provided and are assumed constant. G_{ant} is the receiver antenna gain projected on the surface, σ^0 represents the normalized bistatic radar cross section (NBRCS), R_{rx} is the range from TDS-1 to the specular point, R_{tx} is the range from the GPS transmitter to the

specular point, and χ is the Woodward Ambiguity Function (WAF) that determines the system response for each (τ, f_D) pair. In our case, the SNR observations were always done along the zero-Doppler line ($f_D = 0$).

The WAF can be approximated as the product of a triangular function, resulting from the GPS code auto-correlation function, $\Lambda(\tau)$, and a sinc function, $S(f_D)$, that accounts for the Doppler filtering as a consequence of the coherent integration [28]. The shape of these two functions are determined, respectively, by the positions of the GPS transmitter and receiver satellites, and by their relative velocities.

To decouple the observations from the effects of the receiver and transmitter geometry (the receiver antenna gain and the measurement area), we introduce a correction factor, *CF*, computed for the specular point position. Considering that G_{ant}, σ^0, R_{tx}, and R_{rx} are slowly varying in the vicinity of the specular point, (2) can be approximated as a constant scaling factor in the surface integral of the WAF. Thus, the correction factor can be written as

$$CF_{sp} = \frac{R_{tx}^2(\vec{\rho}_{sp}) \cdot R_{rx}^2(\vec{\rho}_{sp})}{G_{ant}(\vec{\rho}_{sp}) \cdot A}, \tag{3}$$

where $\vec{\rho}_{sp}$ represents the specular point position, and *A* accounts for the effective area in m^2 illuminated on the ocean surface. For the waveform peak, this corresponds to the area enclosed within the intersection of the first chip zone and a sinc function of width 1/*Ti*, where *Ti* is the coherent integration time. For the SGR-ReSI, *Ti*=1 ms, corresponding to a Doppler bandwidth of $\pm$500 Hz. As shown in the Appendix, for incidence angles, θ_i, up to 35°,

this effective area is approximately proportional to $1/\cos^2(\theta_i)$. Considering this approximation, we excluded all points with an incidence angle greater than 35° from our analysis.

The correction factor was then applied to normalize both SNR_{PEAK} and SNR_{WAVE}, resulting in SNR_{PEAK}^{NORM} and SNR_{WAVE}^{NORM}, respectively, as given in (4)

$$SNR_{PEAK}^{NORM} = CF_{sp} \cdot SNR_{PEAK}\,, \tag{4a}$$

$$SNR_{WAVE}^{NORM} = CF_{sp} \cdot SNR_{WAVE}\,. \tag{4b}$$

For the SNR_{PEAK}^{NORM} case, it is straightforward to show that after the application of the correction factor the only contributing terms from (2) are the surface bistatic coefficient, σ^0, and the constant term *K*. The impact of *CF* on the SNR_{PEAK} can be seen in the histograms of SNR_{PEAK} plotted in Fig. 7 before (a) and after (b) the correction factor is applied for different incidence angles. Despite the fact that the transmitted power and antenna gain are not known for the individual GPS transmitters, the spreading of the signal is significantly reduced by applying the *CF* which allows us to use SNR_{PEAK}^{NORM} for ocean parameter sensitivity studies.

The application of CF_{sp} to the whole SNR waveform is justified. As shown in the Appendix, for a given incidence angle (determined by the position of the GPS transmitter and TDS-1), the waveform shape does not change significantly regardless of the relative velocities of the satellites up to a delay corresponding to 6 chips with respect

to the specular point and incidence angles up to 35°. The antenna gain does vary as one moves away from the specular point due to directionality of the antenna beam. However, the antenna gain at the specular point is approximately equal to the average of the gain over the waveform considered in this study where the gain is generally higher at the near-range (between the specular point and the antenna boresight) and lower at the far-range (between the specular point and away from the antenna boresight). Thus, the use of the specular antenna gain in the waveform CF_{sp} calculation is justified with the assumption that the ocean surface conditions are uniform across the illuminated area.

C. DDM Quality Control

It is important to recall that the TDS-1 was launched as a technology risk reduction mission to advance the technical readiness level (TRL) for a variety of hardware on board TDS-1 which included the SGR-ReSI. Because the utilization of the remotely-sensed data to study Earth's environment was a secondary objective, the quality of the data was not at the level that is typically seen from a satellite remote sensing mission. However, the SGR-ReSI measurements are a significant increase from the sparse GNSS-R data that was collected from the UK-DMC mission. Thus, the analysis of SGR-ReSI is a tremendous opportunity to further our understanding of GNSS-R measurements of the ocean surface and provides some risk reduction for the CYGNSS mission.

Proper characterization of any satellite remote-sensing measurement sensitivities to various environmental parameters requires careful data quality control.. One of the largest sources of error in the SGR-ReSI measurements is the geo-location error due to imprecise attitude knowledge provided by the TDS-1 spacecraft. The TDS-1 satellite attitude knowledge comes from an onboard Kalman filter that takes inputs from magnetometers and sun sensors. Attitude knowledge error is estimated to be around 1° in the non-eclipsed part of the orbit and up to 10° when the

satellite is in eclipse [29] [30]. While an “in eclipse” flag is provided in the Level-1 SGR-ReSI data files, we have found it to be erroneous. This study could have been restricted to only daylight SGI-ReSI measurements when the attitude knowledge was derived from the sun sensors, but the available dataset would have been halved. An analysis of the nighttime data showed that while there was more scatter in the dataset it exhibited similar sensitivities as the daytime data. This led us to conclude that the majority of the nighttime data were still good. Careful analysis of the data scatter pointed towards geolocation errors. Measurements contaminated by land or ice exhibit a considerably stronger signal than ocean only measurements. Fig. 8 shows DDMs partially contaminated by sea ice near Antarctica (a), by islands off the Northeastern Australian coast (b), and by an ice sheet in the Nares Strait (c). For comparison, plot (d) shows a DDM retrieved over open ocean. Unmistakably, plots (a-c) are different than plot (d) where the spreading of the horseshoe shape is greatly affected. These examples illustrate why it is important to remove any measurements that might be contaminated by land or ice. To flag ice and land points, we first utilized the conservative land and ice mask from the ECWMF and GDAS weather models. Fig. 9 plots a distribution of the SNR_{PEAK}^{NORM} where the red line shows the dataset before applying the land and ice mask, and the black line shows the dataset after applying the ice and land mask. However, further examination of the dataset revealed points with geo-location errors that were missed using this conservative land/ice mask [7], [31].

The challenge was how to flag the outliers while preserving as much data as possible for subsequent analysis. To accomplish this, we utilized signal sensitivity to wind as our guide and defined a minimum and maximum SNR threshold as a function of wind speed. These thresholds were determined by first calculating the mean SNR_{PEAK}^{NORM} values at 1 m/s wind speed bins. A best-fit curve was then determined for the mean SNR_{PEAK}^{NORM} as a function of wind speed. This curve was used as the shape of the minimum and maximum SNR threshold curves. The minimum and maximum SNR threshold curve offset values were determined through an iterative process of adjusting the curves

downward and upward from the mean SNR_{PEAK}^{NORM}, respectively, with the intent of both retaining as much valid data as possible and minimizing any changes in the SNR_{PEAK}^{NORM} mean behavior. While all wind data sources in the collocation database were utilized in this exercise, we show only the scatter plot of SNR_{PEAK}^{NORM} versus ECMWF wind in Fig. 10a, and Fig. 10b plots the location of the data points that were excluded. The majority of the points in Fig. 10b are located near regions of ice and land or come from data during the eclipse period when the TDS-1 attitude knowledge has the largest errors.

To further ensure that the highest quality DDMs are used in the following sensitivity analysis, SNR_{PEAK}^{NORM} values greater than 0 dB are excluded as well as SNR_{PEAK}^{NORM} values with a receiver antenna gain less than 0 dB. This additional filtering left us with approximately 650,000 data points, or 45% of the original ocean matchup dataset. Restricting the incidence angle range up to 35° also results in an additional 10% of the data being discarded.

D. DDM Incidence Angle Dependence

The geometry of the GNSS-R measurement technique results in SNR measurements over a wide range of incidence angles (see Fig. 11a). Even when restricting the receiver antenna gain to values greater than 0 dB, the incidence angle range still spans between 0-45° (see Fig. 11b). Prior to applying the *CF*, a strong dependence on incidence angle was observed in the SNR_{PEAK} as seen in Fig. 12a. This effect was greatly reduced after the *CF* was applied, however, a residual linear dependence on incidence angle still remained as seen in Fig. 12b. The average behavior of the SNR_{PEAK}^{NORM} as a function of incidence angle and antenna gain is plotted (dB scale) in Fig. 12c and d, respectively. Fig. 12c shows the remaining incidence angle dependence in SNR_{PEAK}^{NORM} after the *CF* is applied. Since we expected some incidence angle dependencies in the geophysical parameters examined, we did not attempt to remove this

residual dependency.

We did not anticipate a gain dependence in SNR_{PEAK}^{NORM} after the *CF* was applied, but the plot in Fig. 12d shows that there is a residual dependence on gain. Since we cannot say with certainty what is causing this remaining dependency, we decided to leave it in the SNR_{PEAK}^{NORM} and characterize the other sensitivities with respect to this residual gain dependence.

III. GNSS-R Sensitivity To Sea Surface Parameters

A. Mean Square Slope, Wind Speed, and Significant Wave Height Relationship

The goal of this study was to characterize the GNSS-R response to the ocean surface by investigating the relationship of the SNR response to ocean surface parameters, such as wind speed, significant wave height (H_s), and the mean square slope (MSS). Using the WW model data, the MSS and H_s correlations with wind speed are first investigated with respect to each of the wind speed sources included in the collocation dataset (e.g., the ECMWF and GDAS models and the ASCAT, RapidScat, and GMI sensors). In Fig. 13, the following are plotted: the 2D histogram of MSS versus wind speed (top row), the H_s versus wind speed (middle row), and the MSS versus H_s (bottom row) utilizing the following wind speed sources (from left to right): ECMWF, GDAS, ASCAT-A/B, Rapidscat, and GMI. Based on these histograms, we conclude that the relationship between the three variables is independent of the wind source utilized.

B. DDM Dependence on MSS, Wind Speed and H_s

The dependence of the GNSS-R signal on MSS, wind speed, and H_s was investigated by examining the changes in SNR_{PEAK}^{NORM} and SNR_{WAVE}^{NORM}. Fig. 14 (a) shows an overlay of the bin-averaged SNR_{PEAK}^{NORM} as a function of ECMWF, GDAS, ASCAT-A/B, RapidScat, and GMI wind speeds. It is interesting to note that the mean SNR_{PEAK}^{NORM} response is essentially identical for all ground truth sources for winds > 7 m/s, and it decreases with increasing wind speed at the rate of 0.09 dB/(m/s). Slight variations in the mean SNR_{PEAK}^{NORM} response are seen at winds < 7 m/s with differences spanning between 1.2 dB at 1m/s to 0.3 dB at 5 m/s. The strongest signal at low winds was obtained when the GMI winds were used as the reference while the weakest signal was observed when ECMWF (black curve) or GDAS (blue curve) model winds were utilized. We attribute this disimilarity to different sensitivities of each wind source in our database to the lower wind speed regime. As noted in [32], the NWP wind speeds probably do not identify areas of low wind speeds properly resulting in more moderate wind observations, which would consequently lower the average SNR_{PEAK}^{NORM} signal. The RapidScat scatterometer operates at the Ku-band wavelength which is more sensitive to lower wind speeds than the C-band wavelength utilized by ASCAT. The mean SNR_{PEAK}^{NORM} curve for RapidScat (green) shows a higher response at low wind speeds than the ASCAT (light blue). The GMI radiometer wind speeds were derived using frequency channels between 10-36 GHz, and the SNR_{PEAK}^{NORM} curve (red) falls somewhere between the ASCAT and RapidScat curves. For moderate wind speed ranges (5-20 m/s), the NWP model winds have a more dynamic range and less variation than the satellite wind products, and the differences in the mean values between NWP model wind products are negligable. At high wind speed speeds, the coarser spatial resolution of the NWP model wind products would be expected to have a lower dynamic range than the satellite wind data. In section II-A, we discussed various factors to consider when utilizing the different wind sources in the high wind speed regime. To examine the general trend of the SGR-ReSI observations with respect to the ocean surface winds, we combined all the wind data together to create a blended wind dataset to investigate the SNR_{PEAK}^{NORM} sensitivity to winds. For each

wind speed bin, the number of samples from each data source was different, and this difference was accounted for by determining the weighted average of each bin. Since we were interested in characterizing the average sensitivity of the SGR-ReSI observations to the winds, we treated each wind data source equally although some data sources might better represent the lower or higher winds than others. It's worth noting that when defining a geophysical model function to relate the SGR-ReSI measurements to the ocean surface wind speed, one might consider how to best utilize the different wind data source sensitivities to low, moderate, and high winds. The resultant mean of the average blended wind is plotted in Fig 14b. The contour lines depict the data density for the combined wind data sources used, and colors on the contours indicate the number of points on a logarithmic scale. At low winds (up to 5 m/s), the signal changes at the rate of approximately 1 dB/(m/s). At moderate winds (5-20 m/s), the rate of change is on the order of 0.2 dB/(m/s), and at high winds (20-35 m/s) an additional total change of about 1.2 dB is seen. Although the number of points for high winds is limited, these preliminary results do lend support for the goal of the future CYGNSS mission to measure winds in tropical cyclones utilizing GNSS-R techniques.

The SNR_{PEAK}^{NORM} versus wind speed behavior changes with incidence angle as seen in Fig. 15. A change of approximately 3 dB is seen over the incidence angle range between 0-35° at a given wind speed, while the sensitivity trend stays the same. A somewhat smaller change is seen at wind speeds < 5 m/s, and it is most likely the result of this study's method of flagging all points where SNR_{PEAK}^{NORM} was larger than 0dB in an attempt to remove land and ice contaminated measurements. The flagging undoubtedly and inadvertently removed some good data points at low winds which would have higher SNR_{PEAK}^{NORM} values.

The impact of significant wave height on the measured SGR-ReSI response to wind was analyzed using the IFREMER WW model and all of the wind speed sources. While this study evaluated sensitivity with respect to each

wind speed source separately and found similar responses, these results use the combined wind speed products discussed previously. Results of this analysis are presented in Fig. 16. The sensitivity of the measured signal to waves is noticable at wind speeds < 10 m/s with changes of 4.5 dB in no wave conditions (black line) to 2.5 dB for waves approaching 5 m (yellow line) in the wind speed range of 3-10 m/s. It is important to note that while this study considers wind and swell waves together, the dominant wave impact at low wind speeds comes from the swell, while at higher wind speeds, it comes from wind generated waves.

To further separate the impacts of waves and winds on the measured signal, we examined waveform changes at constant wind speeds for different H_s levels. The SNR_{WAVE}^{NORM} were bin-averaged into 1 m/s wind speed bins using ECMWF, and 1 m significant wave height bins using the IFREMER WW model. The results for four wind speed bins from 1 to 9 m/s are presented in Fig. 17. In the first column in Fig 17a, we plot SNR_{WAVE}^{NORM} for constant wind speed and different H_s values. The variation between peak values of the waveforms which correspond to different wave heights can be observed. This is consistent with Fig. 16 where the blended wind speed was utilized for analysis. As wind speed increases, the distance between the peaks decreases. To examine if there are any changes in the shape of the waveforms, we scaled the waveforms relative to their peak values and plotted these scaled SNR_{WAVE}^{NORM} in the second column as shown in Fig. 17b. Some spreading of the trailing edges for winds up to 5 m/s is evident. As previously discussed, the application of the *CF* to SNR_{WAVE}^{NORM} is valid up to 6 chips. However, for satellite observations 6 chip delays are far enough from the specular point that wind and wave conditions can be quite different, therefore, this study limited the analysis to a ~3 chip delay. Since some spreading of the waveforms does occur at low winds with a ~3 chip delay, we conclude that it would be possible to utilize the trailing edge to infer additional information about winds and waves. In the third and fourth column (Fig. 17c and d), H_s and MSS are plotted with respect to wind speed within each wind speed bin. No correlation between the wind speed and H_s or MSS exists for the 1-3 m/s

bins which implies that the dominant effects of waves in Fig. 16 and Fig. 17a and b comes from swell. As wind speed increases, the correlation between waves and MSS with wind increases which indicates the formation of locally generated wind waves. We also observe that the spreading of the waveforms gradually diminishes with increasing winds, and that beyond 9 m/s all waveforms start aligning on top of each other.

The mean SNR_{WAVE}^{NORM} as a function of significant waveheight, MSS, and wind speed is presented in Fig 18. The differences in the peak values can be observed in Fig 18a, b, and c (top row). The overall peak-to-peak change is ~3.8 dB for waves up to 5 m, ~5.5 dB for MSS between 0-0.02, and ~7 dB for winds between 1-15 m/s. To study the differences in waveform shapes, we normalized SNR_{WAVE}^{NORM} to its maximum value and plotted it as a function of H_s, MSS, and wind speeds in Fig 18a, b, and c (bottom row), respectively. The spreading in the trailing edge slopes with respect to all three parameters exist at 6 delay chips. As shown in Fig. 18c (bottom), the SNR_{WAVE}^{NORM} at a delay of 6 chips has an increase of ~1.7 dB when the wind speed changes from ~1 to 15 m/s. Fig.14a shows, however, that the SNR_{PEAK}^{NORM} has a 7 dB variation when the wind speed varies from ~1 to 15 m/s. At 6 chips, the changes in the trailing edge are ~1 dB for H_s between 1-6 m, and on the order of 2.1 dB for MSS up to 0.02. Note that although the trailing edge sensitivity is lower, potentially more chips could be used to aid in the retrieval of a particular geophysical parameter of interest. An example of utilizing more chips in the waveform matching retrieval technique is demonstrated in [33].

C. DDM Dependence on SST

The effect of the sea surface temperature (SST) on the measured SGR-ReSI signal was examined using both the GDAS and ECMWF model SSTs as well as NOAA's daily OISST product. This study investigated the SNR_{PEAK}^{NORM} behavior relative to the SST for the individual sources as well as combining the three sources together. No significant difference was observed in SNR_{PEAK}^{NORM} trends between the different SST data sources. To avoid the issue of possible correlation between the wind speed errors and SST in the ECMWF and GDAS models, all of the wind speed sources in the collocation database were used in Fig. 19, which plots SNR_{PEAK}^{NORM} against the OISST stratified by different wind speed bins. The OISST product is independent of the wind speed data sources utilized. There is a noticeable decreasing trend in SNR_{PEAK}^{NORM} from 0 to ~ 2-3° C, which may be caused by ice contaminated data that was not properly flagged out in the collocation database. As the SST increases above 2° C, SNR_{PEAK}^{NORM} increases for wind speeds < 4 m/s with an approximate change of 1.5 dB as the SST varies from 3 to 30° C. Starting at wind speeds greater than ~ 5 m/s, there is an apparent reversal in the slope of SNR_{PEAK}^{NORM} versus SST, where SNR_{PEAK}^{NORM} decreases with increasing SST with a ~0.8 dB change over the SST measurement range. Specifically, the change in dB/°C for each wind speed bin in Fig. 19 is 0.05, 0.047, 0.011, -0.012, -0.015, -0.013, -0.006, and 0.000 for the 0-14 m/s wind speed bins, respectively. Similar behavior was witnessed in both day and night SSTs which suggests this is not a diurnal variability issue. The role of atmospheric stability was also investigated by dividing the dataset into stable and unstable regions based on the differences between the OISST and GDAS model air temperature at a height of 2 m. There were no significant changes in the SNR_{PEAK}^{NORM} behavior versus SST between stable or unstable conditions. The SNR_{PEAK}^{NORM} behavior versus SST for various incidence angle bins and significant wave height bins were also examined and plotted in Fig. 20. The SNR_{PEAK}^{NORM} behavior was similar over the incidence angle range (0-35°) and exhibited a slight rising trend with increasing SST of 0.03 dB/°C for all incidence angles. There was no noticeable trend in the SNR_{PEAK}^{NORM} versus SST behavior as a funciton of significant wave height. While not plotted here, this

study also examined the SNR_{PEAK}^{NORM} response to changing salinity (3-day average SMOS data) and found no apparent sensitivity in this dataset.

D. DDM Dependence on Wind Direction

Theoretical modeling of the bistatically scattered signal [34] shows that the near-peak portion of the waveform exhibits a low dependence to the wave anisotropy (or to the wind direction for wind-driven waves) for specular direction observations. However, Zavorotny *et. al.* [2] showed that a more pronounced dependence exists away from the specular point. Given a 45° incidence angle, an 8 m/s wind speed, and a GNSS-R receiver located at a 10 km altitude, Zavorotny *et. al.*'s [2] theoretical modeling showed a 3 dB difference between the upwind and crosswind waveforms at the time delay of 12 chips (~10-14 km away from the specular point).

SGR-ReSI observations were evaluated with respect to the relative azimuth wind direction using the ECMWF model wind direction. The relative azimuth wind direction was defined as the difference between SGR-ReSI azimuth angle projected in the incidence plane relative to true north and the ECMWF wind direction. Fig. 21a shows a scatterplot of the SNR_{PEAK}^{NORM} as a function of the relative wind direction for wind speeds between 9-10 m/s and a 20-25° incidence angle range. This particular wind speed and incidence angle range was selected because it contained the most data points (11,247 points). The mean SNR_{PEAK}^{NORM} with corresponding error bars was calculated for 10° relative wind direction bins in Fig. 21a. The green curve is a double cosine harmonic fit to SNR_{PEAK}^{NORM} defined by $a0 + a1\cos(\varphi) + a2\cos(2\varphi)$, where φ is relative wind direction. While the dataset does have a bit of scatter, there is a

measureable dependence on the relative wind direction visible in the mean. The SNR_{PEAK}^{NORM} is strongest in the upwind wind direction and weakest in the downwind wind direction with a ~1 dB difference. It is also interesting to note the unimodal nature of the SNR_{PEAK}^{NORM} versus wind direction curve compared to the bimodal NRCS versus wind direction curve commonly found in conventional scatterometer measurements.

We can look at the wind direction dependent behavior away from the specular point in Fig. 21b which plots the SNR_{WAVE}^{NORM} curves at crosswind, upwind, downwind relative wind directions for the 9-10 m/s wind speed bin and a 20-25° incidence angle range. Looking away from the specular point (e.g. at 0.5-1 chip away from the peak power, which is equivalent to ~15 km from the specular point), we observe the difference between how the upwind and downwind SNR_{WAVE}^{NORM} persists and the crosswind SNR_{WAVE}^{NORM} appears to follow the upwind SNR_{WAVE}^{NORM}. This behavior differs from [2] where a 3 dB difference was found between the crosswind and upwind signal. Caution must be used, however, when comparing these two results as the SNR_{WAVE}^{NORM} curves from Fig. 21b were generated strictly along the 0 Hz iso-Doppler line (i.e. essentially corresponding to two points over the annulus zone). In contrast, the results from [2] imply an integration over the complete annulus zone.

IV. Rain Impact

Collocated GMI radiometer and SGR-ReSI measurements were utilized to investigate the impact of rain on the GNSS-R signal. Other radiometers, such as SSMI, SSMI/S, WindSat, and AMSR-2 were considered as possible sources of rain data, but their orbits resulted in few collocations mostly at high latitudes. Fig. 22 shows the distribution of rain rates within the GMI and SGR-ReSI collocation dataset. The majority of the rain rates available for this preliminary analyses were below 2 mm/hr with a limited number of higher rain rate points. SGR-ReSI

operates at the L-Band frequency which has negligible attenuation from rain even for high rain rates, therefore, we do not expect any attentuation impacts. However, rain impacts due to ocean surface modification by rain were observed in the measured L-band radar backscatter signal from the Aquarius scatterometer [35]. Although Aquarius scatterometer measurements are based on different scattering mechanisms than those of SGR-ReSI GNSS-R observations, the surface modification due to rain might be detectable in the GNSS-R measurements. Since the surface modification due to rain is dependent on the wind conditions, we plotted the mean SNR_{PEAK}^{NORM} as a function of wind speed for different rain rate ranges with corresponding error bars in Fig. 23. The last rain bracket represented by the red curve in Fig. 23 contains all rain rates higher than 5 mm/hr. Since satellite winds in our collocation dataset will also be impacted by rain, the ECMWF model wind speed was used as the reference wind speed for this analysis. While there was some spread between the curves, no clear systematic trend was observed with rain as we discerned with a few of the other parameters. The lack of any systematic trend could be attributed to the relatively low rain rates available for analysis, but this can also be attributed to the wind variability that typically exists in the vicinity of rain. For example, [36] shows that the poor quality of ASCAT data in the vicinity of rain is mostly due to the wind variability than rain impacts. The quality of ECMWF winds are also shown to be poor under high wind variability conditions [37]. Considering the fast drop off of the SNR_{PEAK}^{NORM} signal as the wind speed increases as illustrated in Fig. 14, the sensitivity of SNR_{PEAK}^{NORM} signal is highest in low wind regimes, therefore, the small errors in the reported wind speed would result in large signal variations which is what our results show. Therefore, until a substantially larger data set for statistical analysis is available where buoy winds can be used as a validation source, a conclusion whether or not there is any impact of rain on GNSS-R measurements cannot be drawn.

V. Case Studies

In this section, two specific examples of SGR-ReSI measurements are presented to complement the global statistical analysis previously discussed. The first example is a TDS-1 pass over a developing extratropical cyclone just off the southeast tip of Greenland. Extratropical cyclones in this region of the North Atlantic Ocean often result in an enhanced wind flow in the vicinity of the tip of Greenland. This phenomenon is commonly referred to as the Greenland Tip Jet. In Fig. 24, 22:09Z and 23:50Z ASCAT passes as well as an ECMWF model run valid at 00:00Z on January 27, 2015, show the evolution and the size of this storm system. The Z notation refers to Zulu time which is also known as UTC (Coordinated Universal Time). The colored line transecting each ASCAT swath is from a TDS-1 pass at 23:16Z where the colors denote the SNR_{PEAK}^{NORM} values. Along the SGR-ReSI track, the wind speed varied between 10-27 m/s. The DDMs from two points corresponding to wind speeds of 16 m/s and 27 m/s are also shown in Fig. 24. The ocean surface signal response is easily seen in the DDMs at these higher wind speeds indicating there is good sensitivity at these speeds. In Fig 25, SNR_{PEAK}^{NORM} (blue dots), ASCAT retrieved wind speeds (black dots), and a fit to SNR_{PEAK}^{NORM} (green line) are plotted for the entire TDS-1 transect shown in Fig 24. Corresponding ECMWF (red line), GDAS (pink line), and GMI (brown dots) wind speeds are also depicted on the same plot. The SGR-ReSI measurements are inversely proportional to the wind speed where time variations in the measured signal match wind speed trends that indicate good sensitivity of the SGR-ReSI to this range of wind speeds. The large scatter in the SGR-ReSI data can be attributed to the fact that each SNR_{PEAK}^{NORM} observation is taken every 6 km along the track with point resolution varying around 40-50 km depending on the incidence angle with no averaging. For comparison, the ASCAT winds are retrieved every 25 km from NRCS measurements that are averaged for an effective spatial resolution closer to 50 km. It is interesting to note that the spread in the retrieved peak wind speed between all reference sources (ASCAT, ECMWF, and GDAS) are in closer agreement with each

other (28.5 m/s, 24.0 m/s, 25.2 m/s, respectively), while GMI reported a maximum wind speed of 34.6 m/s. The location of the maximum wind does closely agree between all sources, which also aligns with the location of the minimum of the fitted curve. The corresponding scatter plot of the SNR_{PEAK}^{NORM} versus ASCAT-B wind speed is plotted in Fig. 25c. The change in the measured signal is ~2.5 dB for measurements ranging between 10-27 m/s which agrees with mean behavior obtained from our statistical analysis presented in Fig. 14b. The SNR_{PEAK}^{NORM} along the measurement track and corresponding SSTs (from the ECMWF and GDAS models) and OISST are plotted in Fig. 25b. Fig. 25d plots the significant wave height (red) and mean square slope (blue) from WW along the TDS-1 transect where time increases from south to north. As expected, the trend of both parameters is inversely proportional to the observations.

The second case study examines multiple transects over a changing wind field that corresponded with an ASCAT-B pass at 00:23Z on November 16, 2014, and two RapidScat passes at 22:58Z on November 15, 2014, and at 00:43Z on November 16, 2014, which are depicted in Fig. 26. Each transect has an assigned track ID number which represents a series of sea surface reflected signals from a given GPS satellite sensed by the SGR-ReSI receiver. The time series of measured SNR_{PEAK}^{NORM} and of collocated wind speeds from ASCAT-B, GDAS, ECMWF, and RapidScat are plotted on Fig. 27 for each track ID separately. An interesting characteristic of this case is the significant change in the measurement geometry between the different tracks where the incidence angle varied from 9 to 37° and the antenna gain varied from -9.8 dB to 13 dB. In Fig 26, the data from all track IDs is plotted versus the ASCAT-B retrieved wind speed, and is color coded for antenna gain and incidence angle. In these plots, the general trend of decreasing SNR_{PEAK}^{NORM} with increasing wind is observed, but it is also apparent that the incidence angle and location of the specular point in the antenna gain pattern are important factors in the wind speed retrievals where differences in

observational geometry can result in a 8-10 dB difference in the measured signal. This agrees well with our statistical analysis presented in Section III even though measurements with antenna gains less than 0 dB are included in this case study. Measurements with negative gain are depicted with dark blue dots (dark red dots for incidence angle plot) in Fig 26b. The significantly higher signal levels and very large scatter can be observed between those points and the rest of the measurements at winds around 10 m/s. For low winds, the low gain measurements may still have enough signal-to-noise ratio to allow proper wind retrievals. However, for higher winds the observations will most likely need to be omitted. This is consistent with CYGNSS simulation study results presented in [38].

VI. Conclusion

In this paper, we investigated the GNSS-R measurements collected by the SGR-ReSI on board the TDS-1 satellite. The dataset was limited, and required careful quality control procedures which were developed by a thorough analysis of the dataset. In addition, this dataset provided the first opportunity to comprehensively investigate spaced-based GNSS-R sensitivity to ocean surface parameters. The SNR_{PEAK} and the SNR_{WAVE} terms were developed to compensate for the incomplete knowledge of the SGR-ReSI AGC settings and the details of the GPS transmitters. To account for different measurement geometries and antenna gains, a correction factor was computed and used to calculate the SNR_{PEAK}^{NORM} and SNR_{WAVE}^{NORM} terms. However, a small dependence on incidence angle and antenna gain still exists. Quality flagging procedures were also developed to remove data points that were not properly screened by the included quality flags which were largely due to errors in the TDS-1 attitude knowledge caused by the orbit eclipse period. The SNR_{PEAK}^{NORM} and the waveform SNR_{WAVE}^{NORM} sensitivities to the ocean surface winds, waves, sea surface temperatures, wind direction, salinity, and rain were investigated through statistical analysis of a collocation dataset. This datatset collocated the SGR-ReSI measurements with data from other satellite instruments (ASCAT,

RapidScat, and GMI) and numerical models (GDAS, ECWMF, and WaveWatchIII). Case studies were also presented to further illustrate along track signal changes and sensitivities.

The SGR-ReSI measurements exhibited sensitivity through the entire range of wind speeds sampled in this dataset. In the low wind speed range up to 5 m/s, SNR_{WAVE}^{NORM} changes at the rate of approximately 1 dB/(m/s) for a total change of 4 dB. In the moderate wind speed range (5-20 m/s), the rate of change is on the order of 0.2 dB/(m/s) for a total change of 3 dB. In the high wind speed range (20-35 m/s), a rate of change of approximately 0.08 dB/(m/s) for a total change of 1.2 dB was observed. While the number of collocation points with wind speeds above 20 m/s was limited and less weight should be placed upon interpreting the signal strength and intensity in this regime, the observed wind speed sensitivity is encouraging for furture GNSS-R missions.

A significant dependence on swell was observed at lower wind speeds. Independent of the wind speed data source utilized, the sensitivity of the measured signal to swell is significant at wind speeds < 6 m/s, where total changes of 4.5 dB (for no-wave conditions) and 2.5 dB (for waves approaching 5 m) were observed over the wind speed range of 3-10 m/s. It is important to note that while we are considering wind and swell waves together, this study shows that the dominant wave impact at low wind speeds comes from the swell. The impact of the swell waves was noted in the spreading of the trailing edges of scaled waveforms for winds up to 5 m/s. When the waveforms were examined with respect to H_s and MSS, we found that the overall peak-to-peak change is ~3.8 dB for waves up to 5 m, ~5.5 dB for MSS between 0-0.2. At the delay of 6 chips, the differences in the trailing edge of the scaled SNR_{PEAK}^{NORM} increases on the order of ~1.7 dB for wind speeds between ~1 to 15 m/s, ~1 dB for H_s between 1-6 m, and ~2 dB for MSS up to 0.02.

A small functional dependence of the SNR_{PEAK}^{NORM} observations on SST is also noted. For wind speeds less than 4 m/s, SNR_{PEAK}^{NORM} increases by approximately 1.5 dB as the SST varies from 3 to 30° C. Starting at wind speeds greater than ~5 m/s, there is an apparent reversal in the slope of SNR_{PEAK}^{NORM} versus SST, where SNR_{PEAK}^{NORM} decreases with increasing SST with an ~ 0.8 dB change over the SST measurement range.

Our study also revealed a small variation of the SNR_{PEAK}^{NORM} with relative azimuth wind direction. A 1 dB difference in SNR_{PEAK}^{NORM} between the upwind and downwind look direction was observed for wind speeds around 9 m/s and in the 20-25° incidence angle range.

An attempt was also made to examine possible rain impact on GNSS-R observations, however, we may have only detected the impact of wind variability on the SNR_{PEAK}^{NORM} signal in the presence of rain rather than actual rain impact.

While this TDS-1 SGR-ReSI dataset was limited, it was a very significant increase in the available satellite GNSS-R data, and it permitted a much more comprehensive characterization of satellite GNSS-R sensitivities to the ocean surface parameters than previously possible. The knowledge gleaned from this investigation will prove valuable in preparing for the NASA CYGNSS mission which will take exploitation of the GNSS signals to the next level by using a constellation of eight GNSS-R sensors.

VII. Appendix

To assess the effect of the different system parameters on the SGR-ReSI data, and ultimately, to evaluate the use of the *CF* in our data analysis, we computed numerically the mean power waveform model presented in (2) for different geometry scenarios. For our simulations, we considered the bistatic scattering coefficient, σ^0, as a constant value for all the areas under observation, thus concentrating only on the effects of the system parameters, i.e. the antenna gain, the WAF, and the ranges of the transmitter and receiver to the surface. As can be inferred from (2), the received GNSS scattered power is determined by the intersection of these parameters projected on the surface, and the relative weight of each of these zones is determined by the bistatic geometry. For spaceborne receivers, the WAF defines the active scattering area, which makes it the dominating term in the integral. As mentioned above, the WAF is determined by the GPS code auto-correlation function projected on the ground and a sinc function in the Doppler dimension whose width is the inverse of the GPS code coherent integration time. The former is defined by the position of the GPS and LEO satellites (iso-delay lines), and the latter is mostly determined by the LEO satellite velocity (iso-Doppler lines).

To analyze the different geometries, we simulated several scenarios for the GPS and TDS-1 satellites. The orbital height for the GPS satellite was set to 20200 km and to 635 km for the TDS-1. The nominal orbit height and the GPS position was changed along its orbit to obtain the specular point at different incidence angles up to the maximum of the SGR-ReSI field of view (FOV), i.e. 45°. For every satellite geometry configuration, we simulated three cases for the TDS-1 velocity: 1) TDS-1 satellite flying parallel to the incidence plane (this is the plane defined by the GPS, specular point and TDS-1 positions), 2) TDS-1 flying perpendicular to the incidence plane, and 3) TDS-1 velocity at an angle of 45° with respect to the incidence plane. The spacecraft velocity was set to the mean TDS-1 velocity, i.e. 7650 m/s.

The iso-delay and iso-Doppler lines at a 35° incidence angle for the parallel and perpendicular velocity scenarios are provided in Fig. A1(a) and (b), respectively. In the plots, the incidence plane is aligned with the x-axis and is perpendicular to the x-y plane with the specular point located at the origin of coordinates. As mentioned earlier, as we only consider the zero-Doppler beam, the WAF is confined within the ±500 Hz iso-Doppler lines. Thus, for the parallel velocity scenario, as τ increases the WAF expands to successive delay rings mostly along the y-axis at x=0. For the perpendicular velocity scenario, the WAF expands along the x-axis at y=0. Any other TDS-1 velocity orientation with respect to the incidence plane lead to a situation between these two, therefore, as will be shown next, the parallel and perpendicular velocities result in the greatest difference in active scattering areas for the same incidence angle.

A. The Active Scattering Area Contributing to the DDM Peak

Let us consider now how the active scattering area changes as a function of the incidence angle for different TDS-1 velocity directions considered here. In this section, we consider only DDM maximum (τ = 0, f_D = 0) which corresponds to the area around the specular point position on the surface. This area is delimited by the first chip zone and by the ±500 Hz iso-Doppler lines.

To compute the active scattering area, we evaluate (2) with all the parameters in the equation set to a value of 1 except for the WAF. As shown in Fig. A2(a), the active area around the specular point increases with incidence angle as the iso-delay and iso-Doppler lines move away from each other. It can also be observed that the areas increase differently depending on the velocity orientation with the parallel and perpendicular velocity scenarios leading to the most dissimilar results. In the plot, we also show the $1/\cos^2$ curve that is mostly coincident with the perpendicular velocity case.

In Fig. A2(b), we present the difference in dB of the normalized areas with respect to the $1/\cos^2(\theta_i)$ curve.

In the worst-case scenario, the maximum variation in the peak is 0.7 dB at an incidence angle of 35° for the parallel velocity scenario. However, this is a very particular case, and according to our calculations it is expected that more than 80% of SGR-ReSI observations considered in our analysis will have a maximum *CF* error smaller than 0.3 dB. Therefore, we consider $1/\cos^2(\theta_i)$ as a good approximation for the variation with incidence angle of the active scattering area around the specular point.

B. Model Waveform Numerical Computation

To evaluate the effect of *CF*, we computed the model waveform in (2), and applied the normalization factor as expressed in (3). For the antenna gain, we used a synthetic antenna radiation pattern with a beam-width of 30° to simulate the SGR-ReSI beam. In Fig. A3(a), we show the waveforms normalized by the peak power of the nadir case for different incidence angles and for the parallel (solid lines) and perpendicular (dashed lines) velocity cases. When *CF* is not applied, the peak power dynamic range due only to the geometry variations would make the estimation of geo-physical parameters unachievable. In Fig. A3(b), we show the waveforms after applying the correction factor, *CF*. The waveform peak differences are linked to the variations in active scattering area as explained in the previous section. It is also observed that the difference in the normalized waveforms is fairly constant up to 6 delay chips. We, therefore, consider that for the analysis presented in this paper it is justified to apply a constant *CF* for all waveforms based on the *CF* computed for the specular point position.

VIII. Acknowledgement

The authors wish to acknowledge the support of the NASA CYGNSS project and NOAA Ocean Remote Sensing Program for this effort.

IX. References

[1] J. L. Garrison, S. J. Katzberg and M. I. Hill, "Effect of sea roughness on bistatically scattered range coded signals from the Global Positioning System," *Geophys. Res. Lett.,* vol. 25, no. 13, pp. 2257-2260, 1998.

[2] V. U. Zavorotny and A. G. Voronovich, "Scattering of GPS signals from the ocean with wind remote sensing application," *IEEE Trans. Geosci. Remote Sens.,* vol. 38, no. 2, pp. 951-964, 2000.

[3] S. Gleason, "Remote Sensing of Ocean, Ice and Land Surfaces Using Bistatically Scattered GNSS Signals From Low Earth Orbit," *Ph.D. thesis, University of Surrey,* 2006.

[4] M. P. Clarizia, "Analysis of gnss-r delay-doppler maps from the uk-dmc satellite over the ocean," *Geophysical Research Letters,* vol. 36, no. 2, 2009.

[5] P. Jales and M. Unwin, "Mission Description - GNSS Reflectometry on TDS-1 with the SGR-ReSI," Surrey Satellite Technology Limited, 2015.

[6] C. Ruf, A. Lyons, M. Unwin, J. Dickinson, R. Rose, D. Rose and M. Vincent, "Cygnss: Enabling the future of hurricane prediction [remote sensing satellites]," *Geoscience and Remote Sensing Magazine, IEEE,* vol. 1, no. 2, pp. 52-67, 2013.

[7] G. Foti and C. Gommenginger, "TDS-1 GNSS-R winds: Inversion & early validation," in *TechDemoSat-1 User*

Consultation Meeting: Coean Winds and Waves Monitoring with GNSS-Reflectometry, National Oceanography Centre, Southampton, UK, March 5, 2015.

[8] S. Soisuvarn, F. Said, Z. Jelenak and P. S. Chang, "Evaluation and Validation of Simulated CYGNSS Winds over Large Range of Tropical Cyclones," in *GNSS+R Workshop*, Potsdam, 2015.

[9] "ASCAT Product Guide," EUMETSAT, July 2015. [Online]. Available: http//www.eumetsat.int/website/home/Data/RegionalDataServiceEARS/EARSASCAT/index.html.

[10] "National Aeronautics and Space Administration, ISS-RapidScat," Jet Propulsion Laboratory, California Institute of Technology, [Online]. Available: http://www.jpl.nasa.gov/news/fact sheets/issrapidscat factsheet.pdf.

[11] F. Wentz, T. Meissner, C. Gentemann, K. Hilburn and J. Scott, "Remote Sensing Systems GCOM-W1 AMSR2 Daily Environmental Suite on 0.25 deg grid, Version 7.2," 2014. [Online]. Available: http://www.remss.com/missions/amsre.

[12] F. Wentz, T. Meissner, J. Scott and K. Hilburn, "Remote Sensing Systems GPM GMI Daily Environmental Suite on 0.25 deg grid, Version8.1," 2015. [Online]. Available: http://www.remss.com/missions/gmi.

[13] F. Wentz, K. Hilburn and D. Smith, "Remote Sensing Systems DMSP SSMI/I Daily Environmental Suite on 0.25 deg grid, Version 7," 2012. [Online]. Available: http://www.remss.com/missions/ssmi.

[14] F. Wentz, L. Ricciardulli, C. Gentemann, T. Meissner, K. Hilburn and J. Scott, "Remote Sensing Systems Coriolis Windsat Daily Environmental Suite on 0.25 deg grid, Version 7.0.1," 2013. [Online]. Available: http://www.remss.com/missions/windsat.

[15] H. L. Tolman and e. al., "User manual and system documentation of WAVEWATCH III version 4.18," NOAA, 2014. [Online]. Available: http://polar.ncep.noaa.gov/waves/wavewatch/manual.v4.18.pdf.

[16] N. Rascle and F. Ardhuin, “A global wave parameter database for geophysical applications. part 2: Model validation with improved source term parameterization,” *Ocean Modelling*, vol. 70, pp. 174-188, 2013.

[17] A. Roland and F. Ardhuin, “On the developments of spectral wave models: numerics and parameterizations for the coastal ocean,” *Ocean Dynamics*, vol. 64, no. 6, pp. 833-846, 2014.

[18] N. Rascle, “Personal Communication,” March, 2016.

[19] S. Soisuvarn, Z. Jelenak, P. S. Chang, S. O. Alsweiss and Q. Zhu, “CMOD5.H-A high wind geophysical model function for C-band vertically polarized satellite scatterometer measurements,” *IEEE Trans. Geosci. Remote Sens.*, vol. 51, no. 6, pp. 3744-3760, 2013.

[20] N. Ebuchi, “Evaluation of marine vector winds observed by RapidScat on the International Space Station using Statistical Distribution,” in *IGARSS*, 2015.

[21] L. Ricciardulli, T. Meissner, J. P. Scott and F. J. Wentz, “Satellite-based Ocean Vector Wind Climate Data Record,” in *AGU Fall Meeting*, San Francisco, CA, 2015.

[22] F. J. Wentz, L. Ricciardulli, T. Meissner and D. Smith, “New Satellite Wind Climatology from QuikSCAT, WindSat, AMSR-E and SSM/I,” in *International Ocean Vector Winds Science Team Meeting*, Annapolis, MD, 2011.

[23] T. Meissner and F. J. Wentz, “Wind-vector retrievals under rain with passive satellite microwave radiometers,” *IEEE Trans. Geosci. Remote Sens.*, vol. 47, no. 9, pp. 3065-3083, 2009.

[24] I. A. Refrew, G. N. Peterson, D. Sproson, G. W. K. Moore and H. Z. S. Adiwidjaja, “A comparison of aircraft based surface layer Observations Over Denmark Straigt and the Irminger Sea with Meteorological Analysis and QuikScat winds,” *Quarterly Journal of the Royal Meteorological Society*, 2009.

[25] T. Meissner, L. Ricciardulli and F. Wentz, “The RSS WindSat Version 7 All Weather Wind Vector Product,”

in *International Ocean Vector Winds Science Team Meeting*, 2010.

[26] P. Jales, "MERRByS Product Manual - GNSS Reflectometry on TDS-1 with the SGR-ReSI," Surrey Satellite Technology Limited, 2015.

[27] C. Ruf, P. Chang, M. Clarizia, S. Gleason, Z. Jelenak, J. Murray, M. Morris, S. Musko, D. Posselt, D. Starkenburg and V. Zavorotny, CYGNSS Handbook, Ann Arbor, MI: Michigan Pub, Apr 2016.

[28] S. J. Katzberg, J. Dunion and G. G. Ganoe, "The use of reflected GPS signals to retrieve ocean surface wind speeds in tropical cyclones," *Radio Science,* vol. 48, pp. 371-387, 2013.

[29] G. Foti, C. Gommenginger, P. Jales, M. Unwin, A. Shaw, C. Robertson and J. Rosello, "Spaceborne GNSS-Reflectometry for ocean winds: First results from the UK TeckDemoSat-1 mission," *Geophys. Res. Lett.*, vol. 42.

[30] G. Foti, C. P. Gommenginger, P. Jales, M. Unwin, A. G. P. Shaw, Y. C. Robertson and J. Rosello, "Preliminary analyses and validation of new spaceborne GNSS-Reflectometry data from the UK TechDemoSat-1 mission for ocean wind retrieval," in *IGARSS*, Milan, Italy, 2015.

[31] G. Foti, C. Gommenginger and M. Unwin, "Preliminary analyses and validation of new spaceborne GNSS-R data from the UK Techdemosat-1 mission for ocean wind retrieval," in *GNSS+2015*, Potsdam, Germany, 11-13 May 2015.

[32] F. J. Wentz and D. K. Smith, "A model function for the ocean-normalized radar cross section at 14 GHz derived from NSCAT observations," *Journal of Geophysical Research,* vol. 104, no. C5, pp. 11,499-11,514, 1999.

[33] F. Said, S. Soisuvarn, S. Katzberg, Z. Jelenak and P. S. Chang, "Estimation of maximum hurricane wind speed using simulated CYGNSS measurements," in *Geoscience and Remote Sensing Symposium (IGARSS)*, Milan,

2015.

[34] A. G. Voronovich and V. U. Zavorotny, “Full-Polarization Modeling of Monostatic and Bistatic Radar Scattering From a Rough Sea Surface,” *IEEE Trans. on Antennas and Propagation*, vol. 62, no. 3, pp. 1362-1371, 2014.

[35] W. Tang, S. Yueh, A. Fore, G. Neumann, A. Hayashi and G. Lagerloef, “The rain effect on Aquarius’ L-band sea surface brightness temperature and radar backscatter,” *Remote Sens. Environ.*, vol. 137, pp. 147-157, 2013.

[36] W. Lin, M. Portabella, A. Stoffelen and A. Verhoef, “ASCAT Wind Quality Control near Rain,” *IEEE Trans. Geosci. Remote Sens.*, vol. 53, no. 8, pp. 4165-4177, 2015.

[37] M. Portabella, “Rain effects on ASCAT wind retrieval: Towards an improved quality control,” *IEEE Trans. Geosci. Remote. Sens.*, vol. 50, no. 7, pp. 2495-2506, 2012.

[38] F. Said, S. Soisuvarn, Z. Jelenak and P. S. Chang, “Performance assessment of simulated CYGNSS measurements in the tropical cyclone environment,” *IEEE Journal of Selected Topics in Applied Earth Observations and Remote Sensing*, pp. 1-11, 2016.

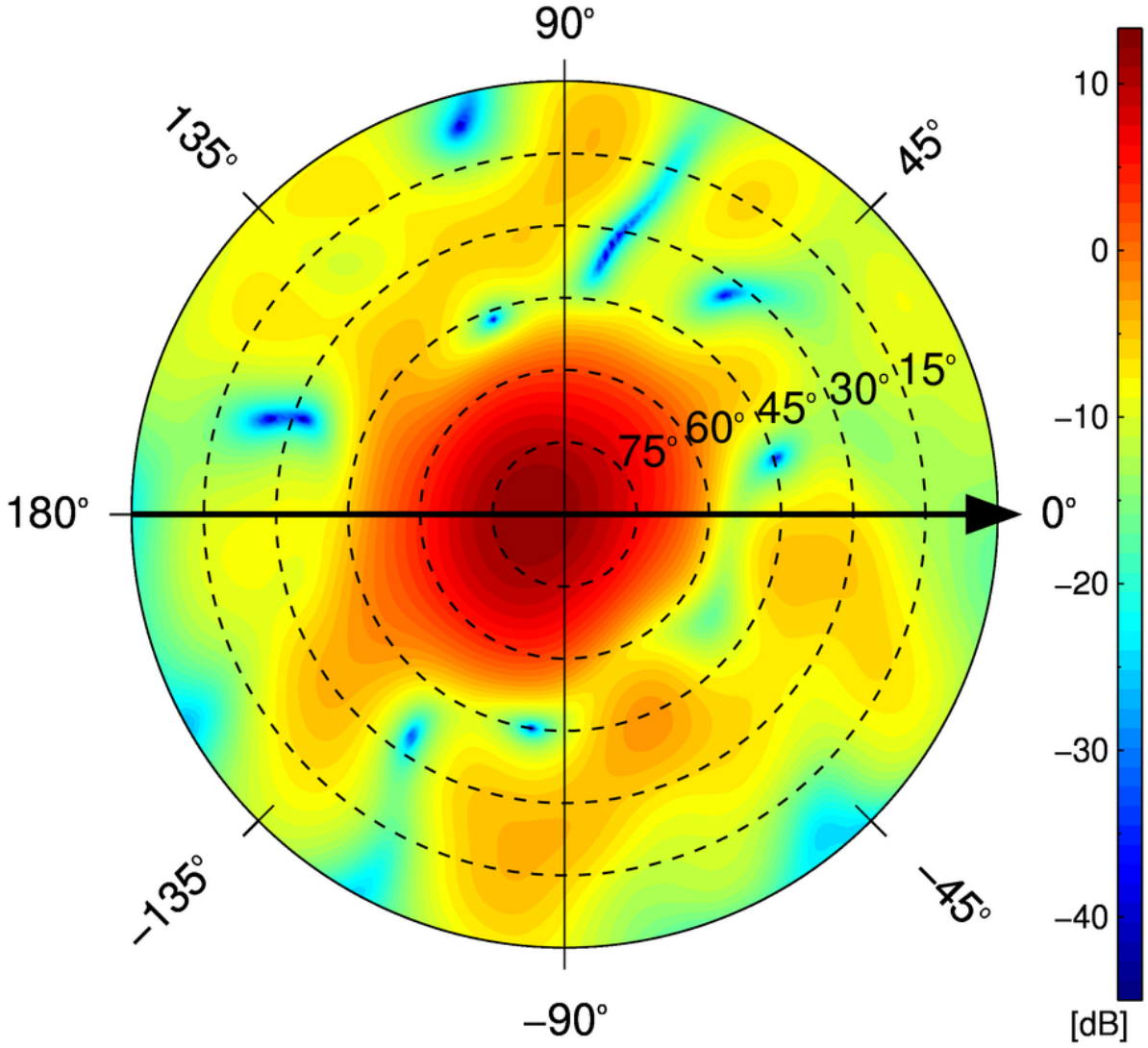

Fig. 1. TDS-1 SGR-ReSI antenna pattern projected on the surface of Earth as a function of azimuth and elevation angles.

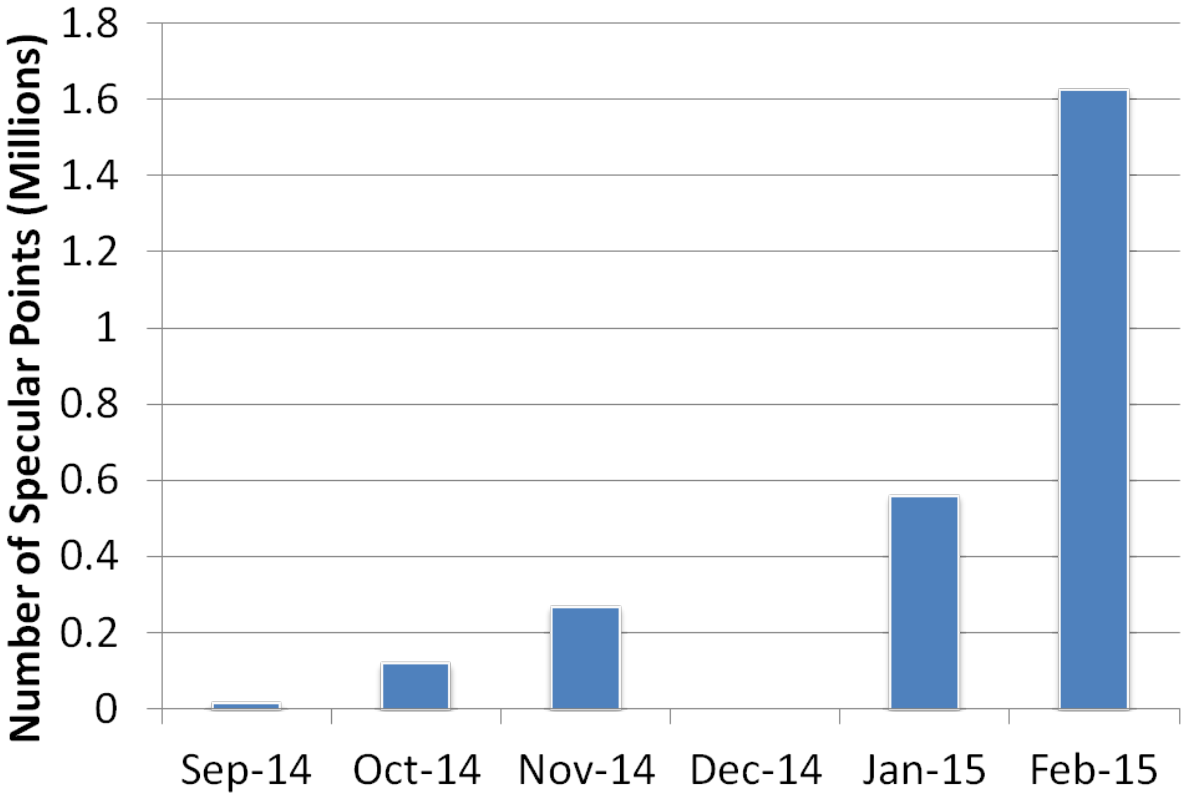

Fig. 2. Released TDS-1 SGR-ReSI data on the MERRByS site as of July 2015. The plot shows the total number of observations acquired during each continuous collection sequence. In 2014, the actual days of observation are Sep 01; Oct 06, 14, 30-31; Nov 08, 15-17, 23. In 2015, the observation days are Jan 26-28; Feb 03-05, 11-13, 19-21.

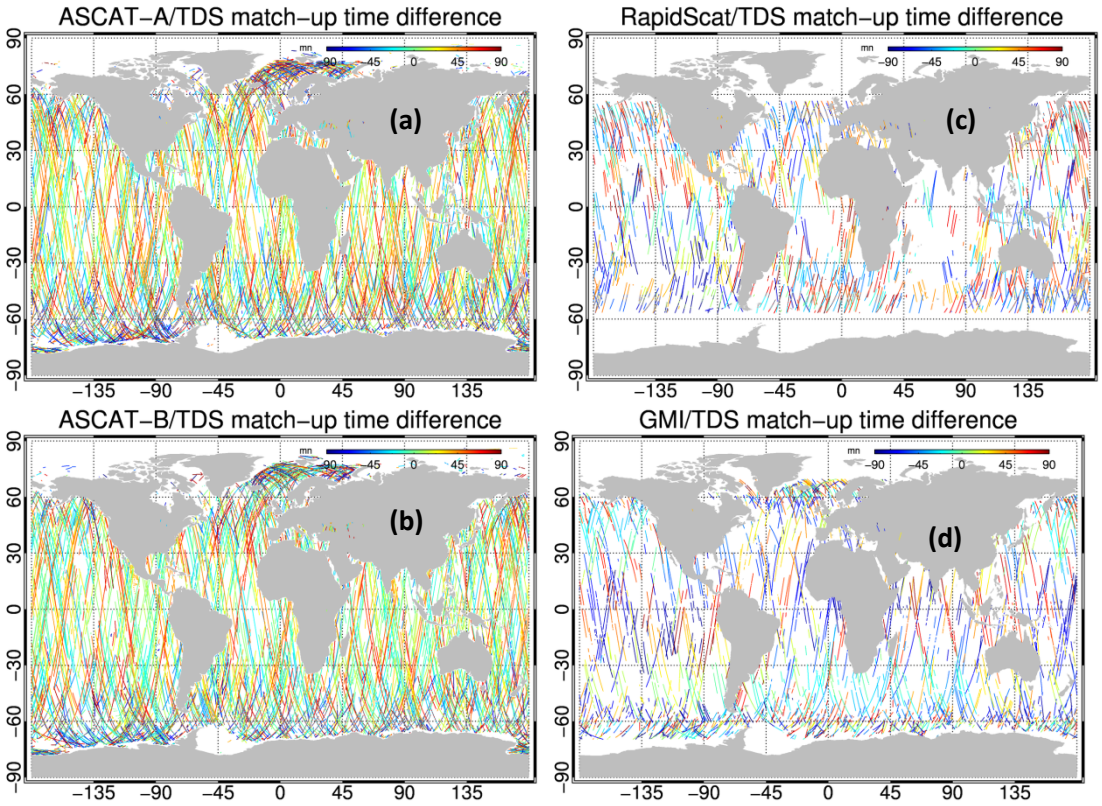

Fig. 3. Collocated TDS-1 SGR-ReSI locations with the ASCAT-A (a), ASCAT-B (b), RapidScat (c), and GMI (d) sensors where the time differences between measurements are depicted as different colors.

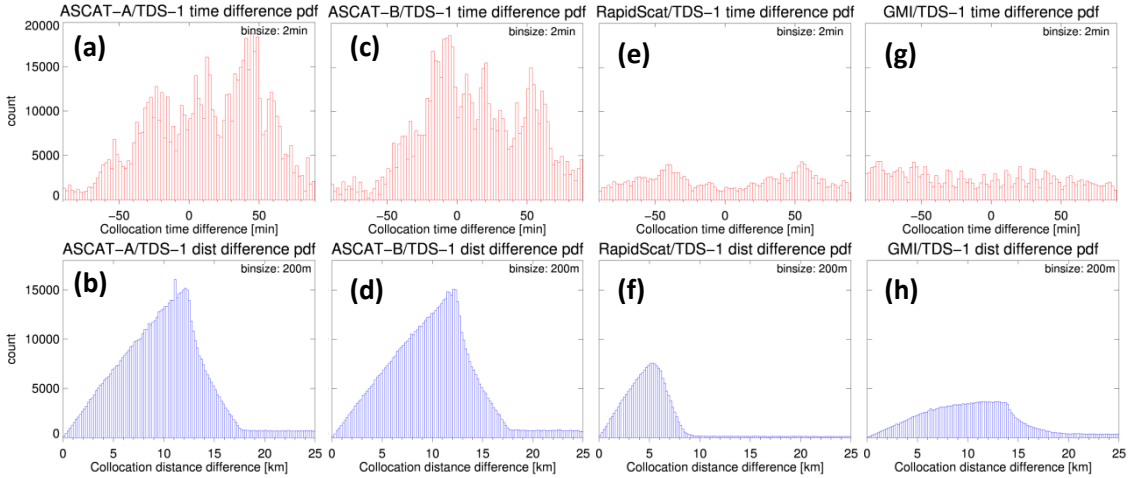

Fig. 4. Histograms of the time and space differences between TDS-1 SGR-ReSI and the ASCAT-A (a-b), ASCAT-B(c-d), RapidScat (e-f), and GMI (g-h) sensors.

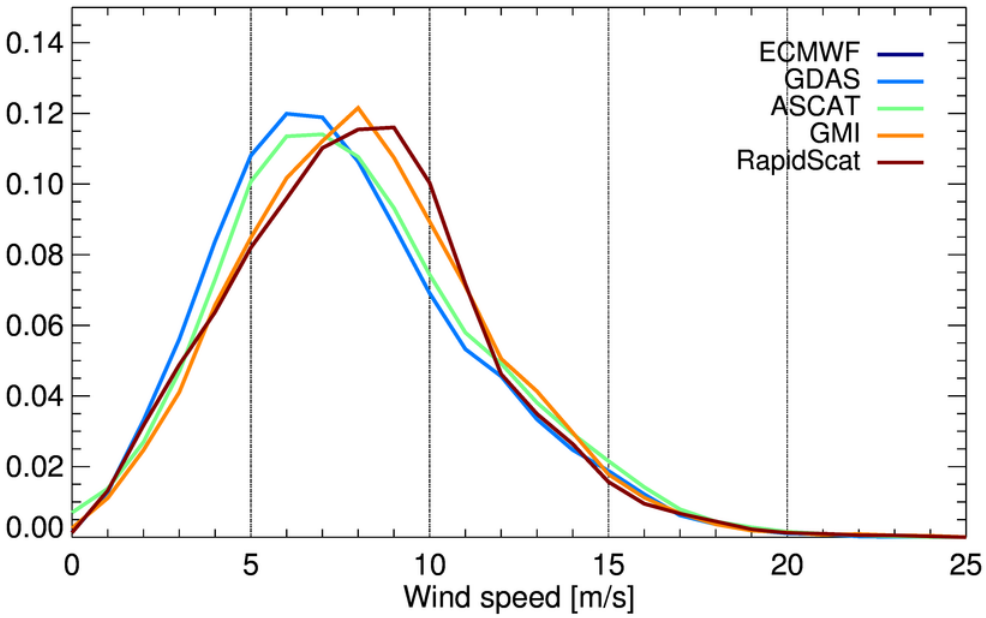

Fig. 5. Wind speed PDF of collocated data of SGR-ReSI with ECMWF, GDAS, ASCAT, GMI, and RapidScat.

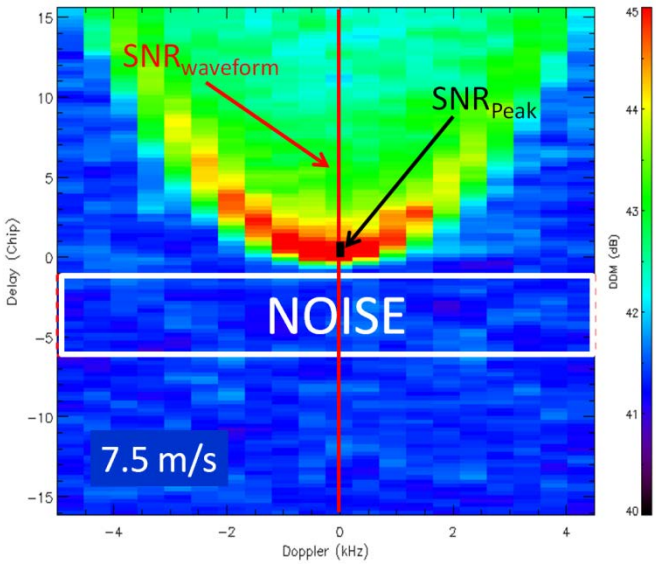

Fig. 6. The DDM signal-to-noise ratio is computed using Equation (1) where the <*Noise*> is the average of the noise within the white box. The black dot represents the location of the peak power used in SNR_{PEAK}^{NORM} calculations, and the red line represents the 0 Hz Doppler line along which the normalized power-vs.-delay waveform SNR_{WAVE}^{NORM} was calculated.

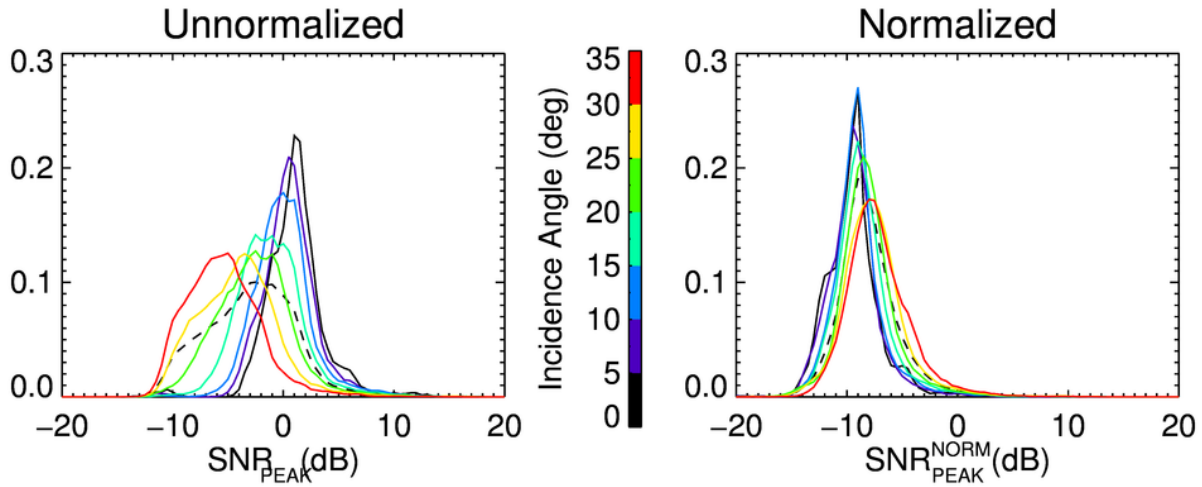

(a) (b)

Fig.7. The PDF of SNR_{PEAK} before normalization (a) and after the correction factor, *CF*, is applied (b).

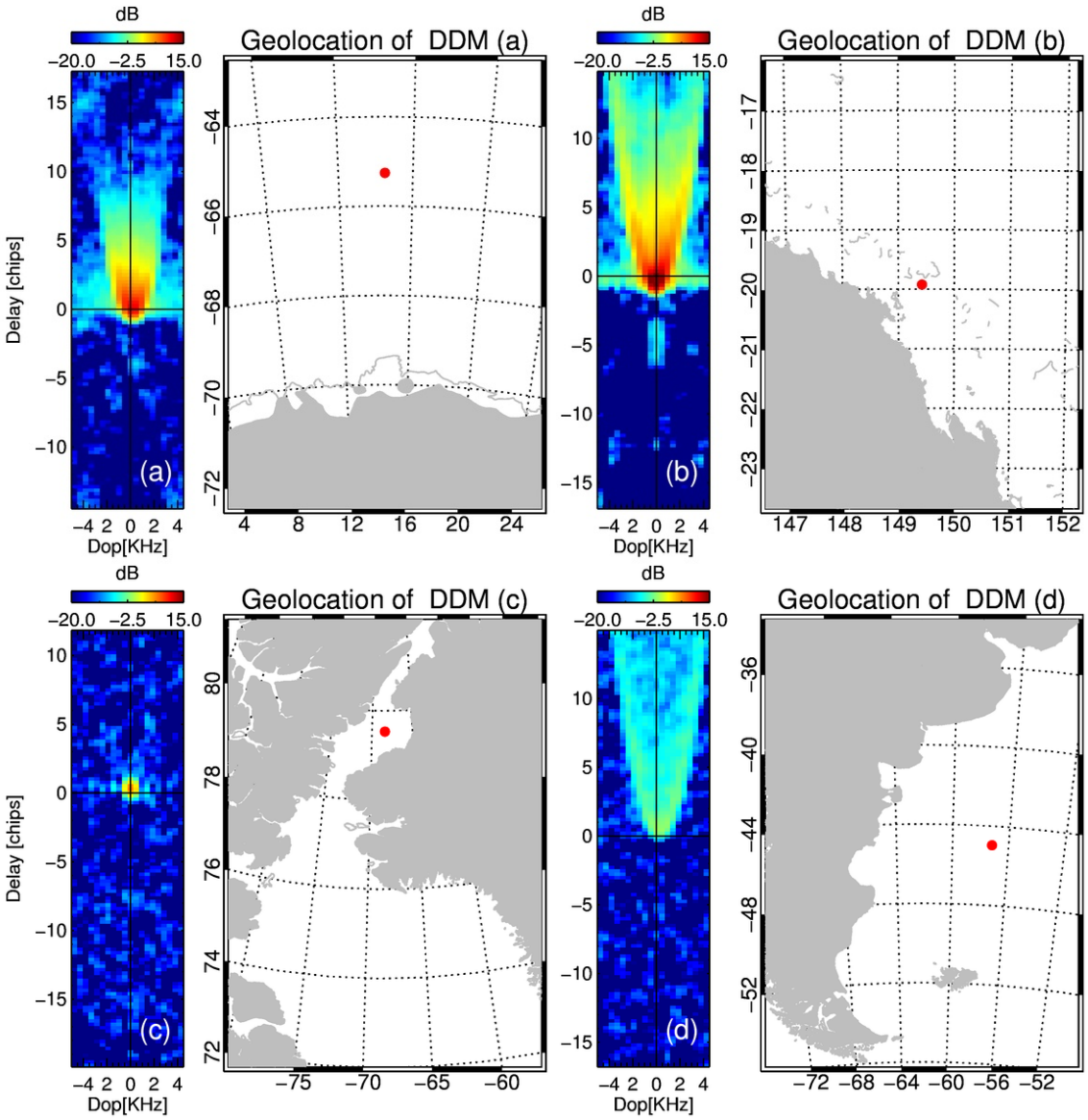

Fig. 8. Examples of DDMs identified as most likely contaminated by sea ice (see DDM (a)), and by islands off the Northeastern Australian coast (see DDM (b)). Plot (c) shows a DDM retrieved over an ice sheet. For comparison, plot (d) shows a DDM retrieved over open ocean. The data measurement times are Jan 26, 2015, at 22:21 UTC, Jan 26, 2015, at 23:34 UTC, Feb 03, 2015, at 19:14 UTC, and Jan 28, 2015, at 02:02 UTC for DDMs a through d, respectively. Note that the shown DDMs are normalized using (1).

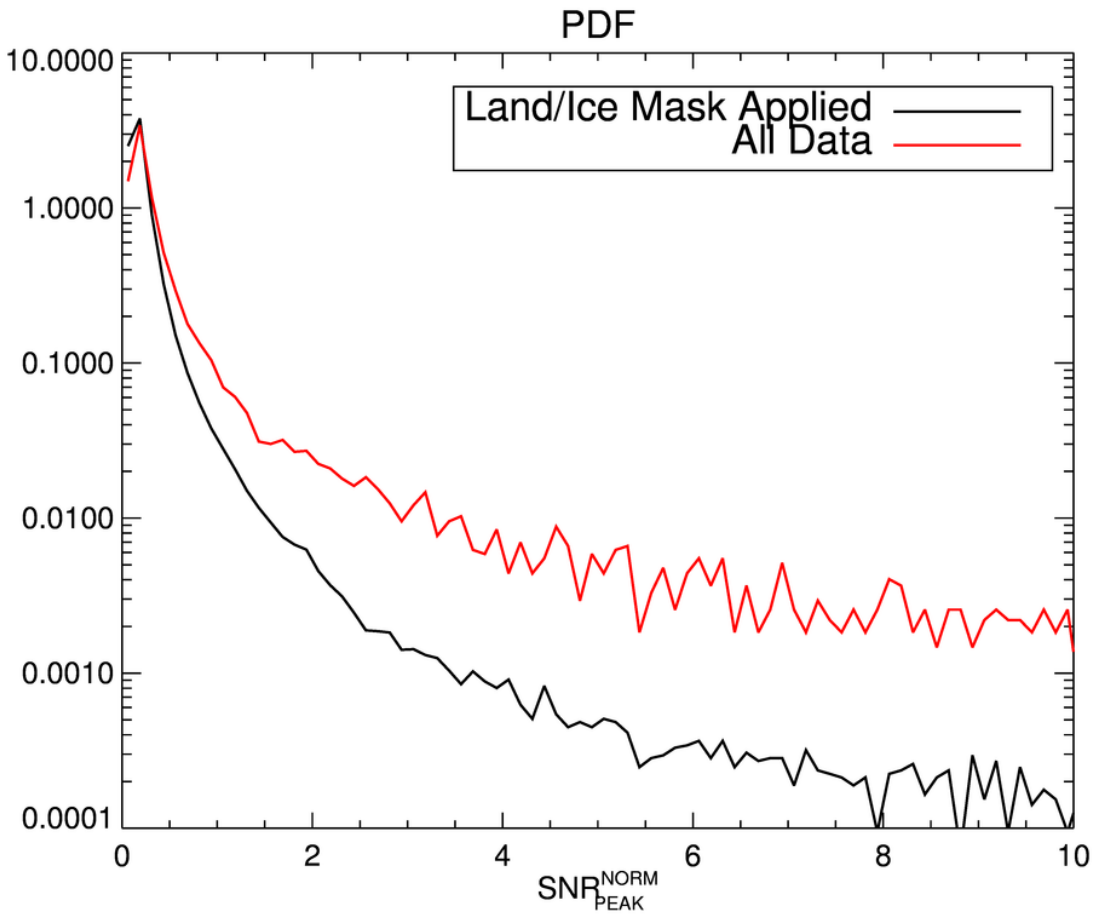

Fig. 9. Normalized SNR_{PEAK}^{NORM} probability density function of data that includes measurements affected by land/ice (red line) and ocean only data after the land/ice flag was applied (black line).

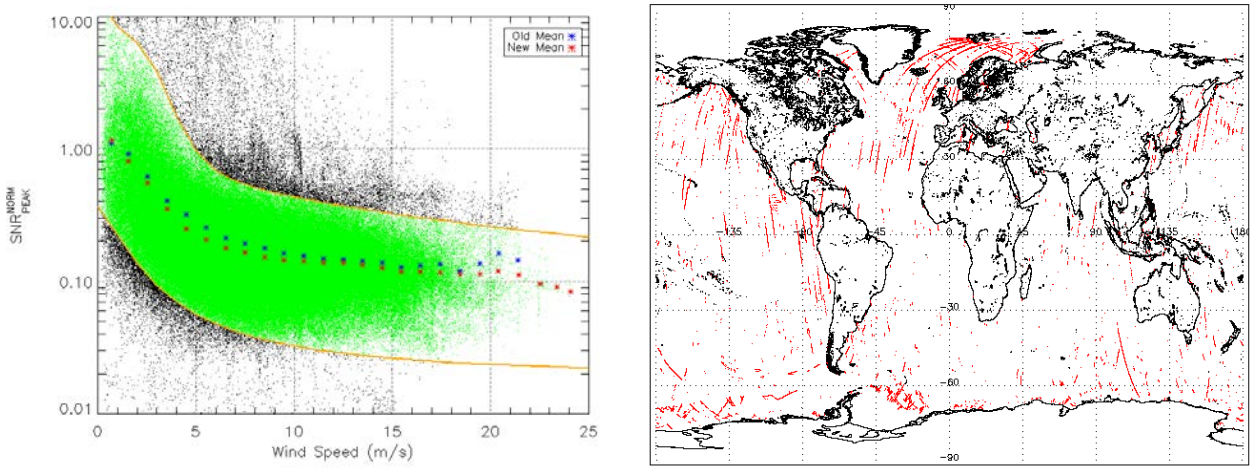

(a) (b)

Fig. 10. (a) SNR_{PEAK}^{NORM} vs. the ECMWF wind speed with the out of bounds data quality flag depicted by the upper and lower yellow lines, respectively. The green points indicate the good data, and the red points depict the new SNR_{PEAK}^{NORM} mean. (b) The geographic locations of the out of bound data points.

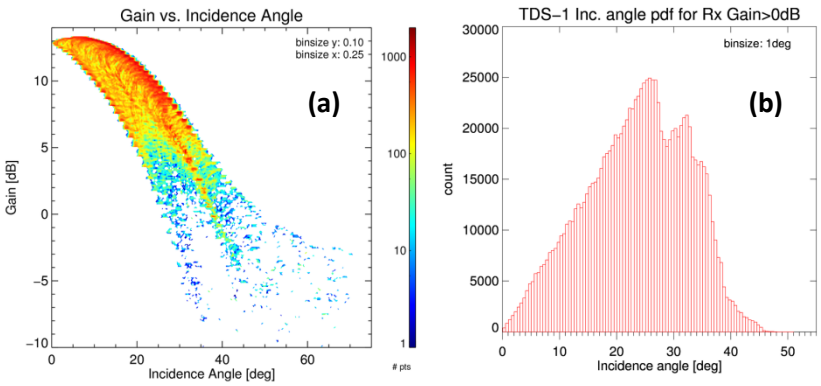

Fig 11. (a) 2D histogram of the TDS-1 SGR-ReSI incidence angle and gain distribution. (b) The incidence angle histogram for antenna gains > 0dB.

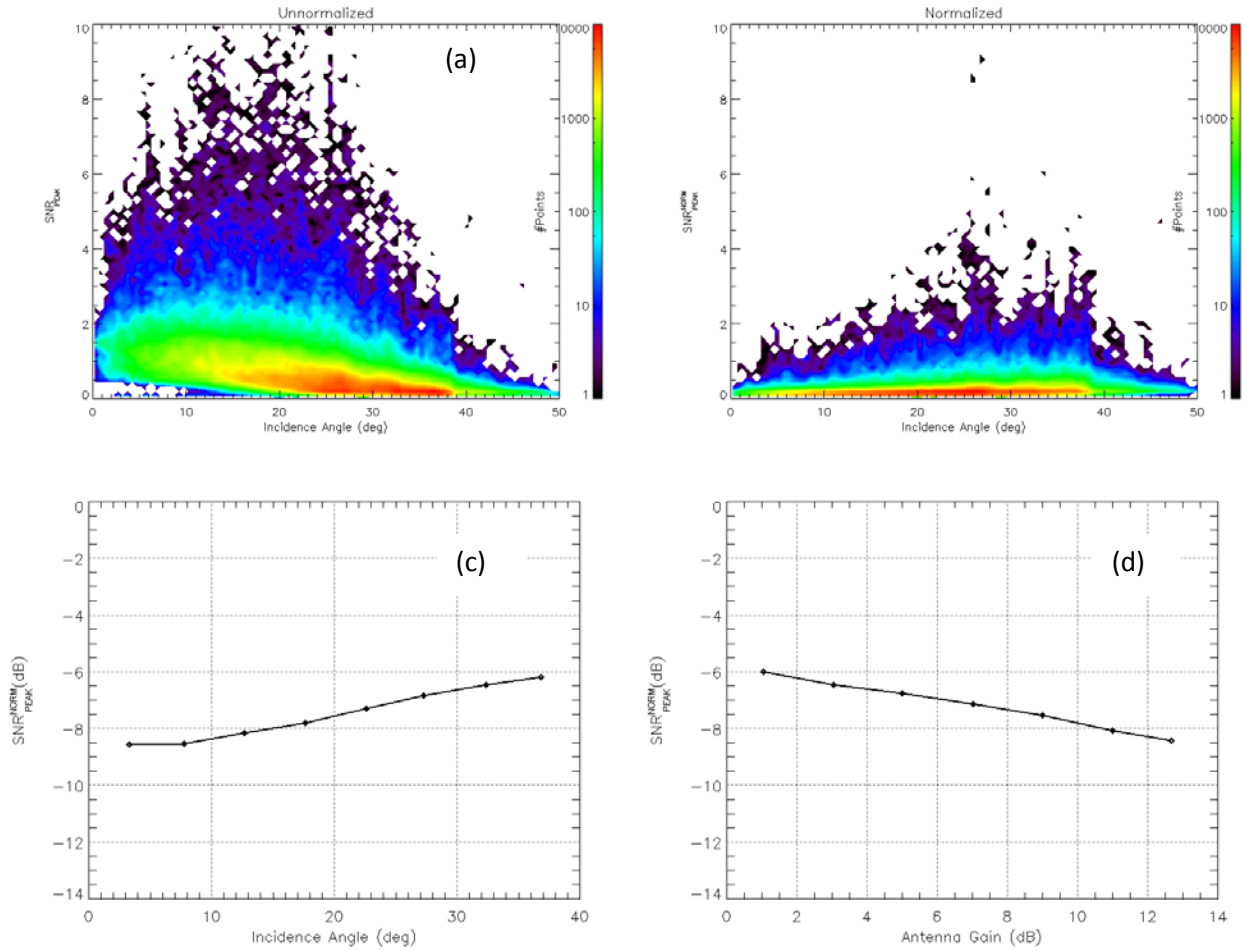

Fig. 12. (a) The 2D histogram of the SNR_{PEAK} shows a strong incidence angle dependence. (b) The 2D histogram of SNR_{PEAK}^{NORM}. Note that both plots (a) and (b) use a linear scale for SNR. The average SNR_{PEAK}^{NORM} behavior over the entire incidence angle range (c) and antenna gain range (d).

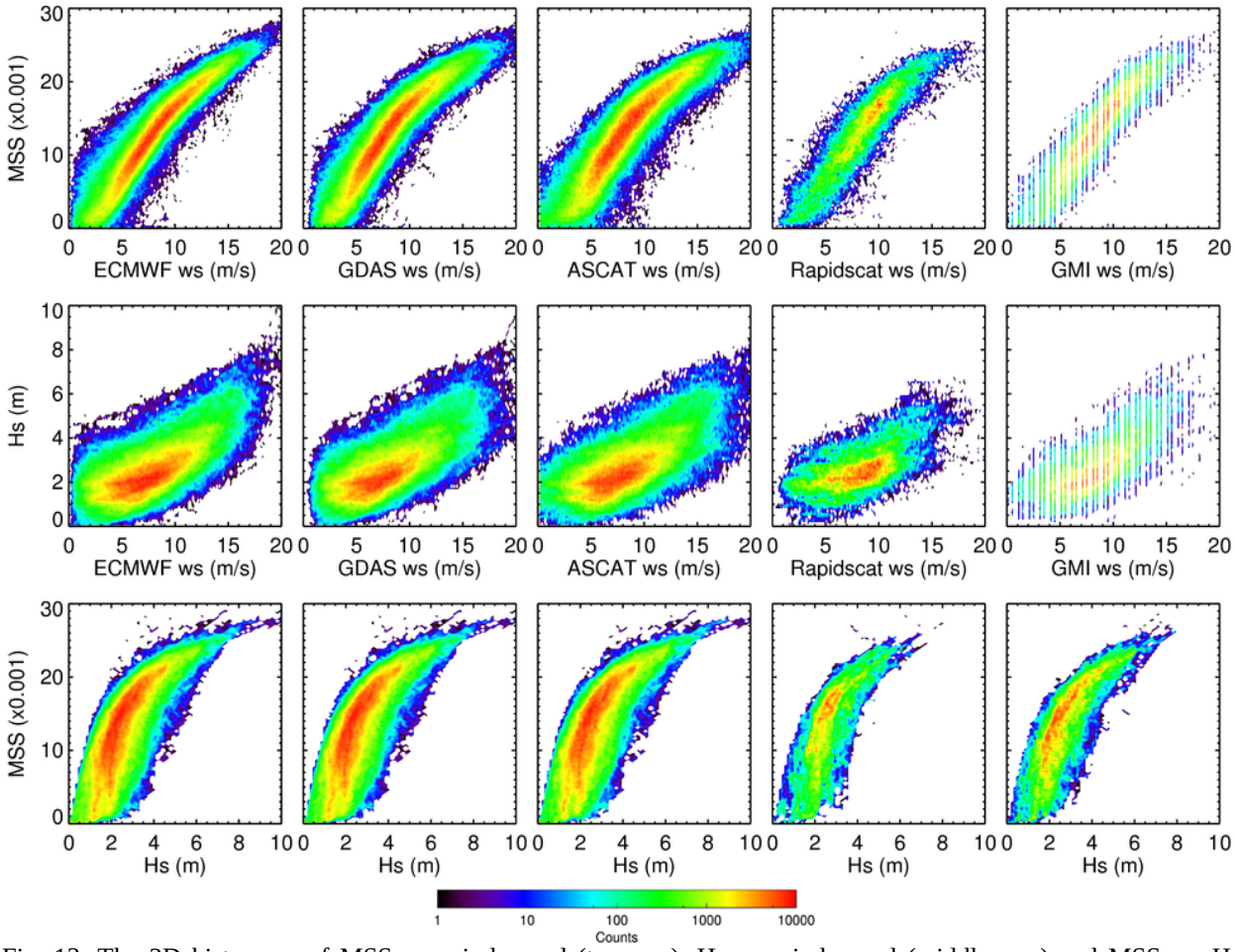

Fig. 13. The 2D histogram of MSS vs. wind speed (top row), H_s vs. wind speed (middle row) and MSS vs. H_s (bottom row) utilizing wind speed sources (from left to right): ECMWF, GDAS, ASCAT-A, ASCAT-B, RapidScat, and GMI for all plots.

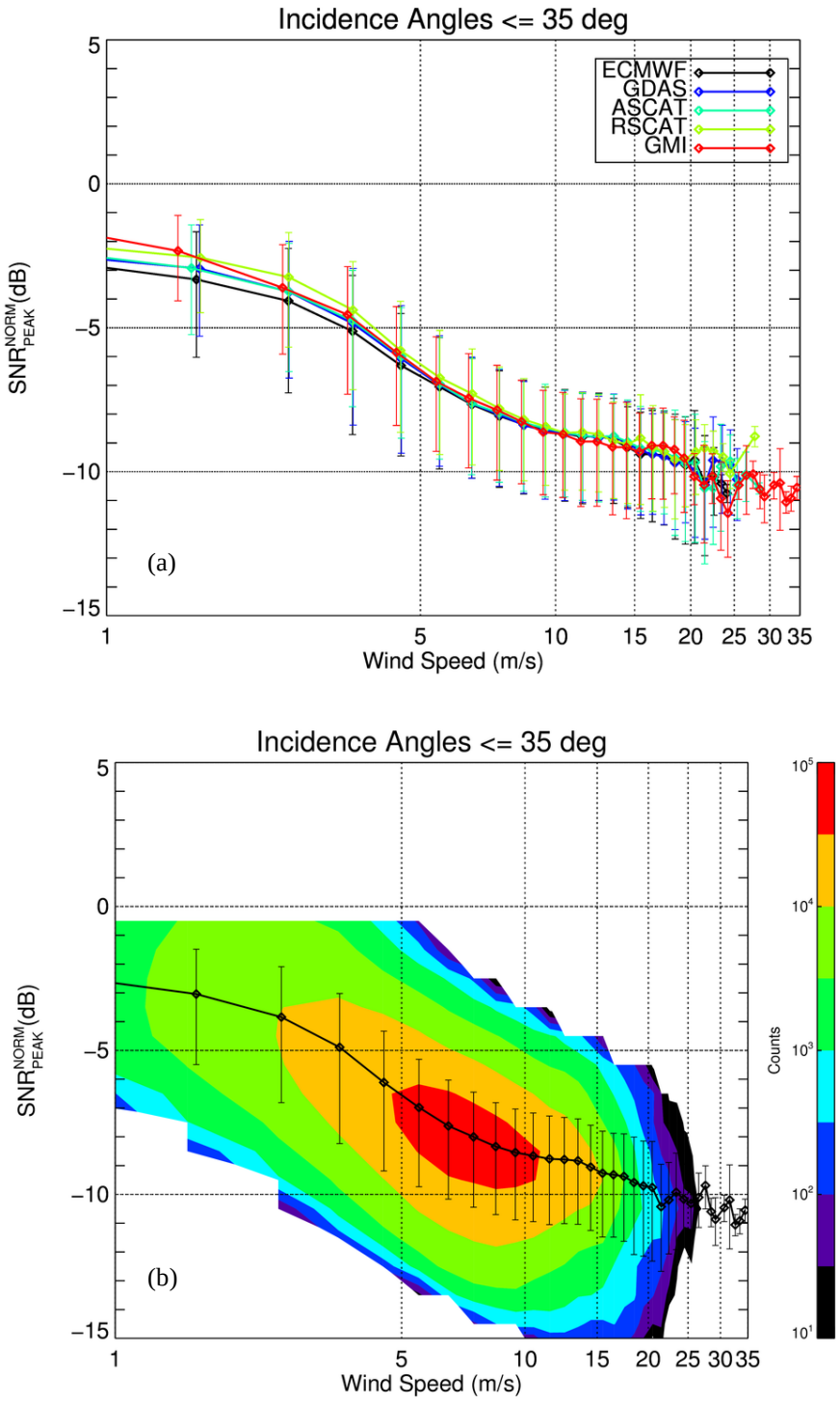

Fig. 14. (a) SNR_{PEAK}^{NORM} vs. wind speed for each wind speed source in the collocation database. (b) Scatter plot of SNR_{PEAK}^{NORM} vs. wind speed presented as a contour plot and corresponding the SNR_{PEAK}^{NORM} vs. the mean wind speed (black line). The reference wind speed on the plot represents combined wind speed from all sources in our collocation dataset.

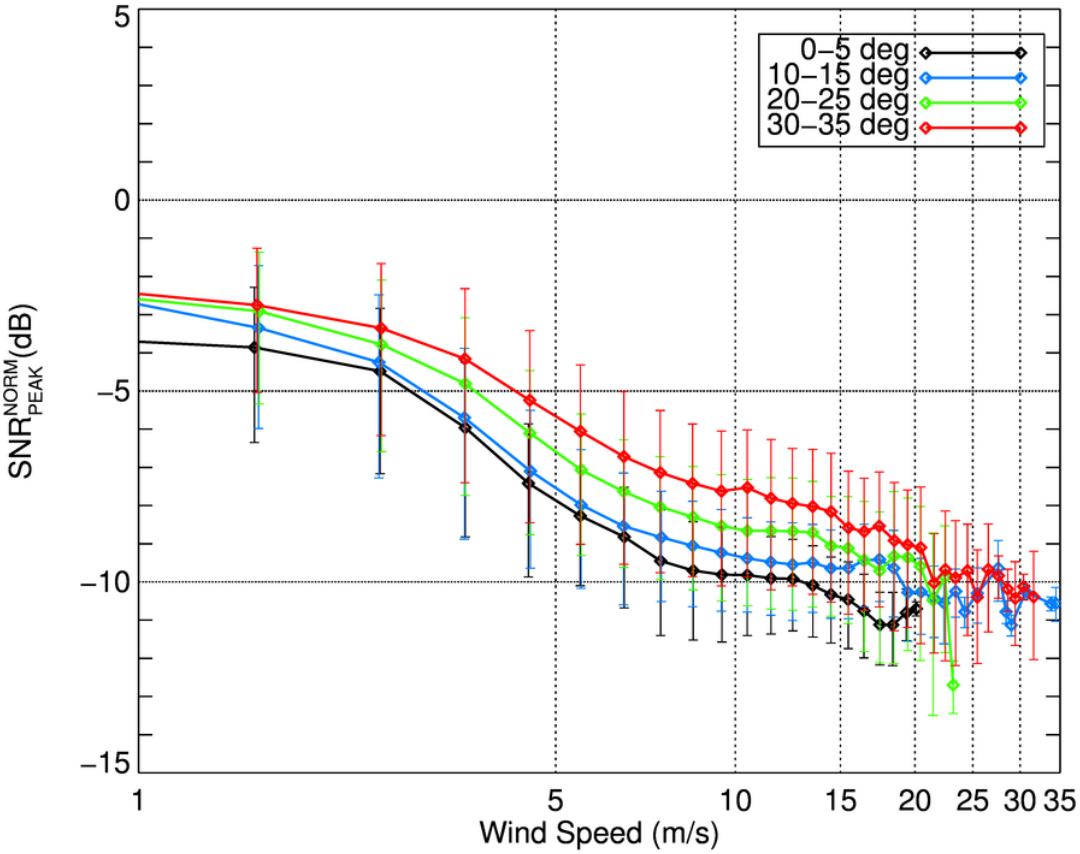

Fig. 15. SNR_{PEAK}^{NORM} vs. wind speed as a function of incidence angles.

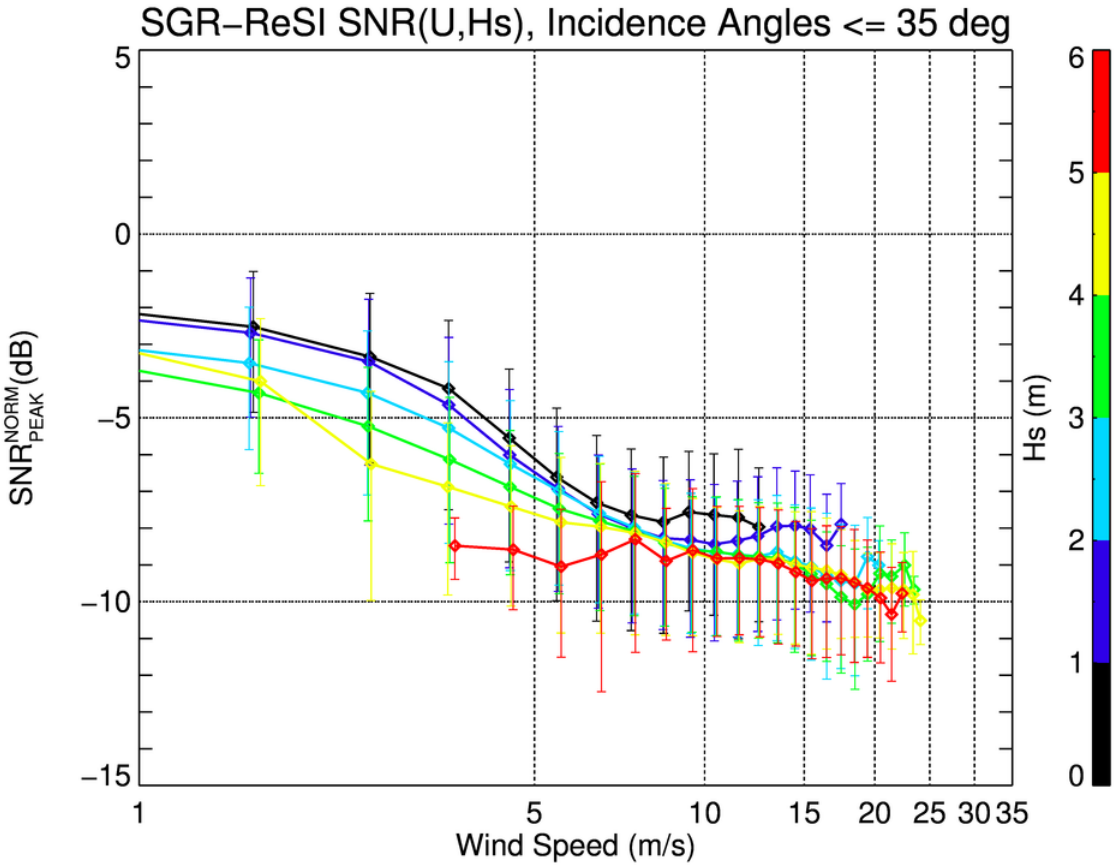

Fig. 16. SNR_{PEAK}^{NORM} dependence on the significant wave height (Hs) as a function of wind speed.

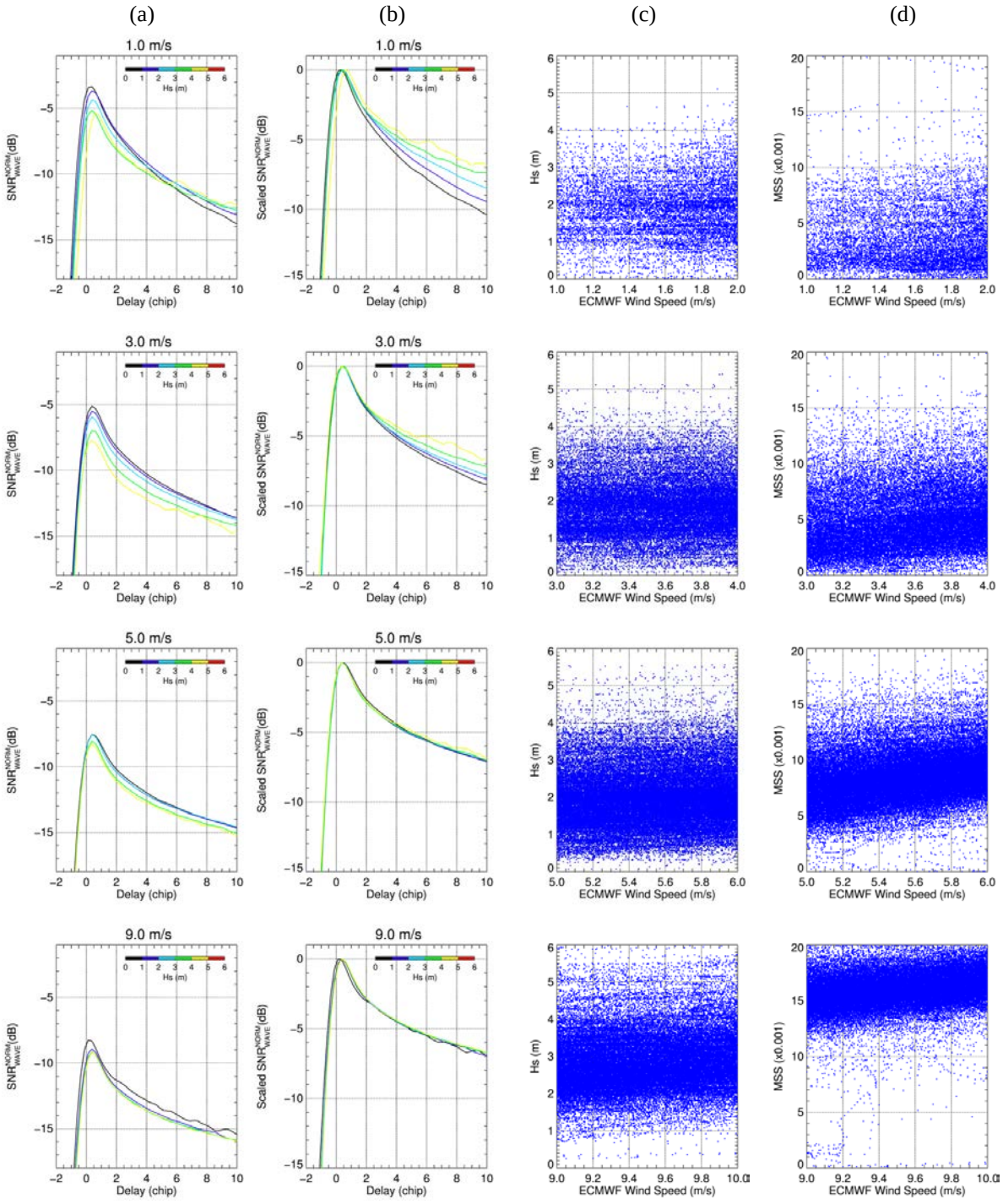

Fig. 17. Assessment of the impact of swell to the SNR_{WAVE}^{NORM}. Plots from columns (a) and (b) show the SNR_{WAVE}^{NORM} and the scaled SNR_{WAVE}^{NORM}, respectively, for 1-2, 3-4, 5-6, and 9-10 m/s wind speed bins as a function of the significant wave height. Plots from columns (c) and (d) show the corresponding scatter of Hs and MSS, respectively, as a function of wind speed.

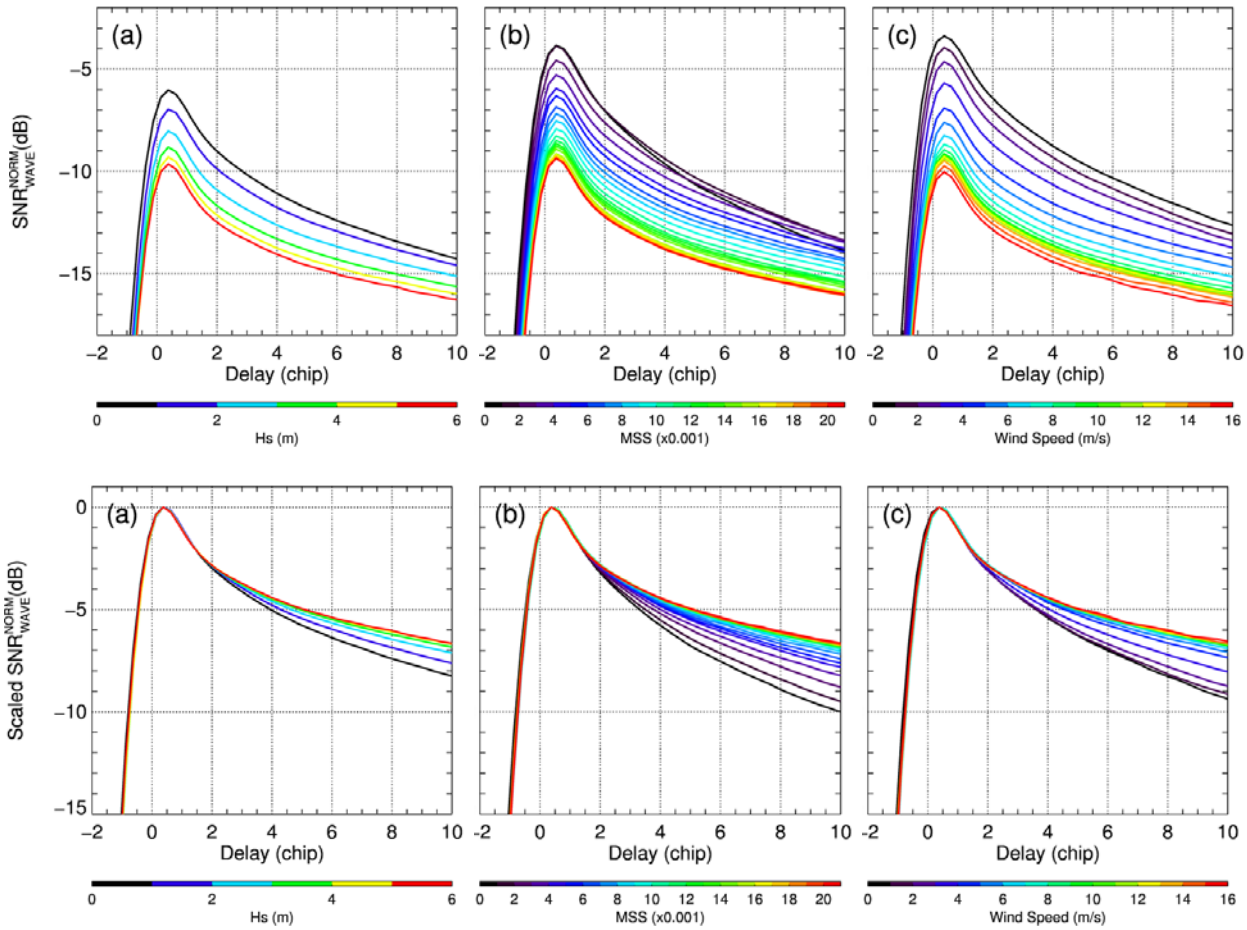

Fig. 18. The SNR^{NORM}_{WAVE} plotted as a function of (a) Hs, (b) MSS, and (c) Wind Speed (top row) and the corresponding scaling waveforms at the peak respectively (bottom row).

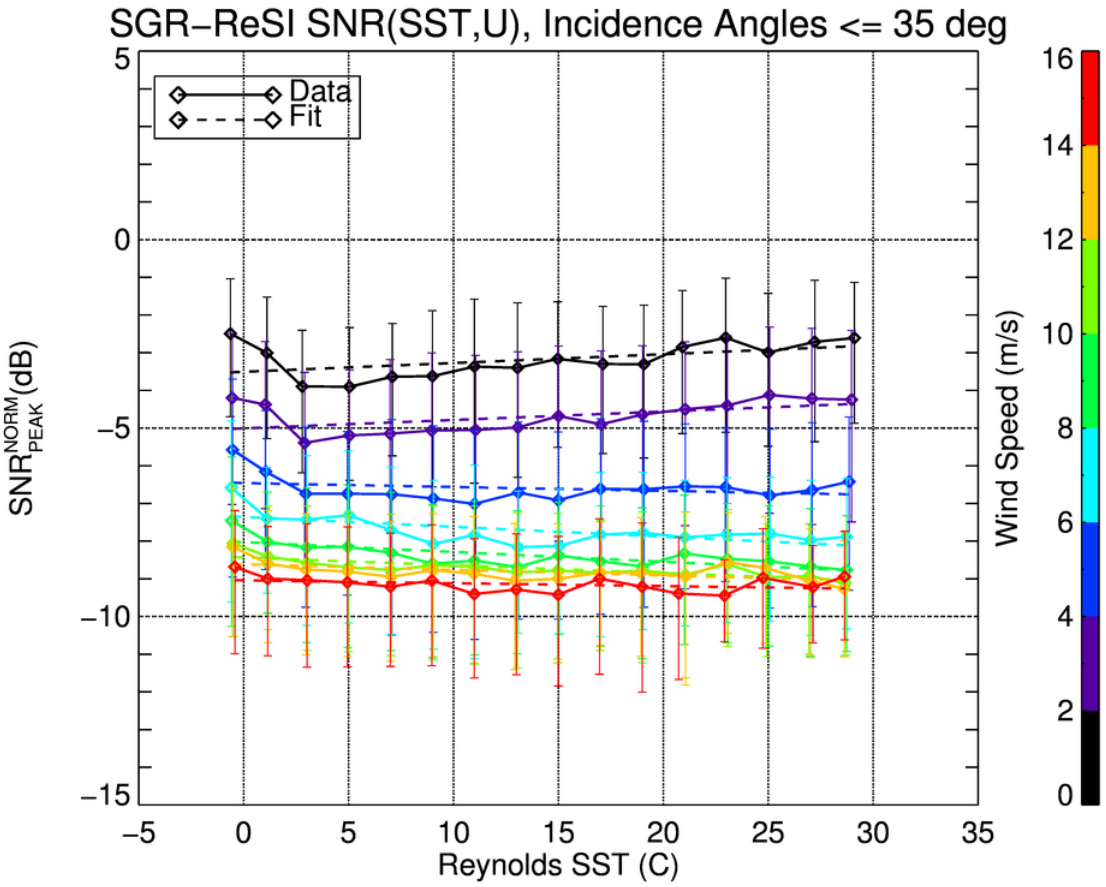

Fig. 19. Sea surface temperature sensitivity of SNR_{PEAK}^{NORM} as a function of wind speed.

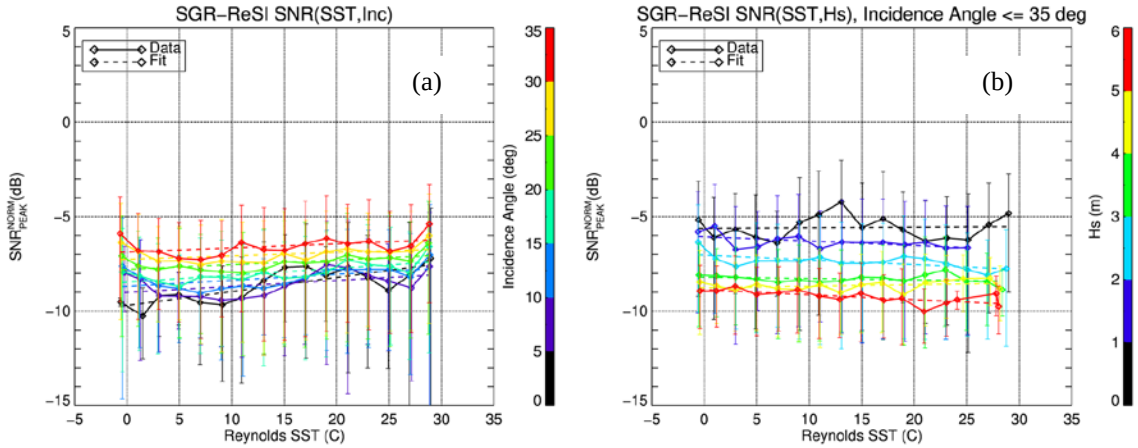

Fig. 20. The sensitivity of SNR_{PEAK}^{NORM} to sea surface temperature (SST), and (a) incidence angle and (b) significant wave height.

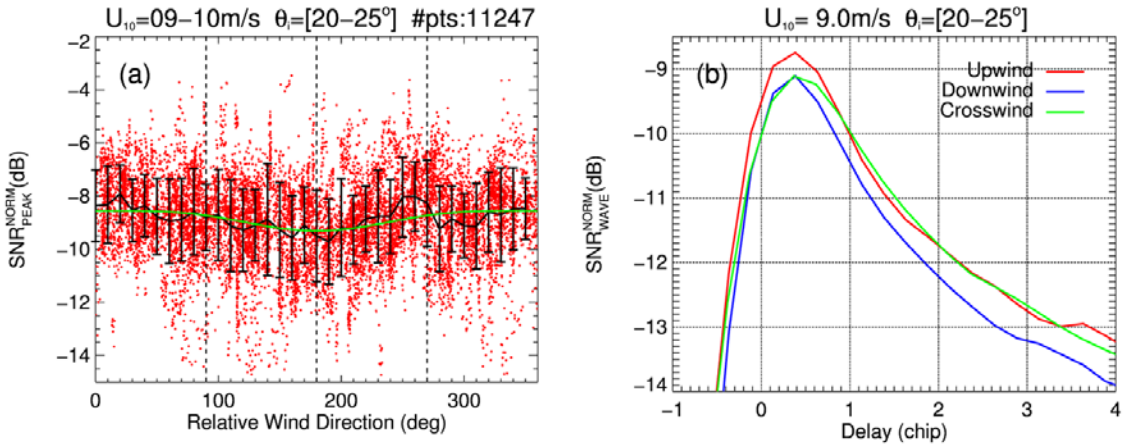

Fig. 21. Scatterplot of the SNR_{PEAK}^{NORM} as a function of the relative wind direction given a 9-10 m/s wind speed and 20-25° incidence angle ranges (see plot (a)). The black curve represents the bin averaged SNR_{PEAK}^{NORM} (10° bin size) with the corresponding standard deviation shown with error bars. The green curve is a sinusoidal fit to the data. Plot (b) shows the SNR_{WAVE}^{NORM} curves at crosswind, upwind, and downwind relative wind directions for the 9-10 m/s wind speed bin and a 20-25° incidence angle range.

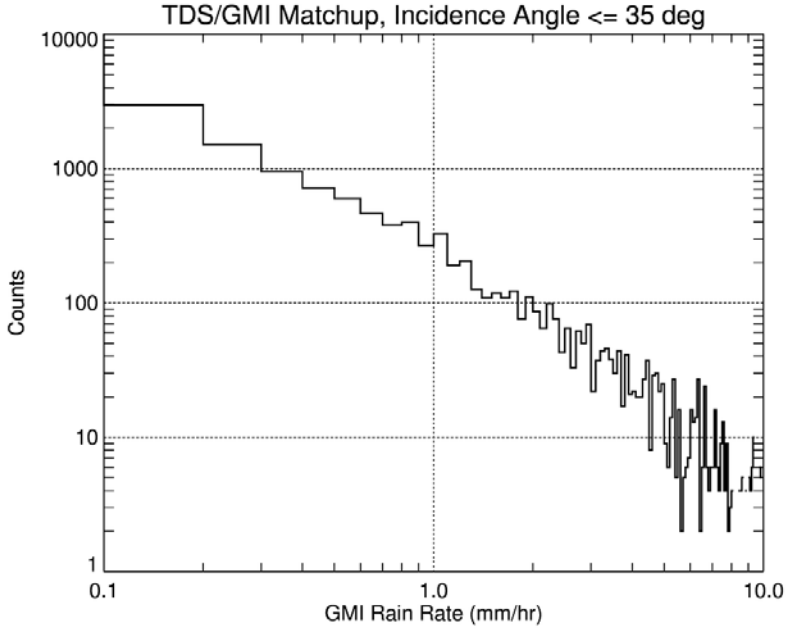

Fig. 22. The GMI rain rate distribution in TDS-1 collocation dataset.

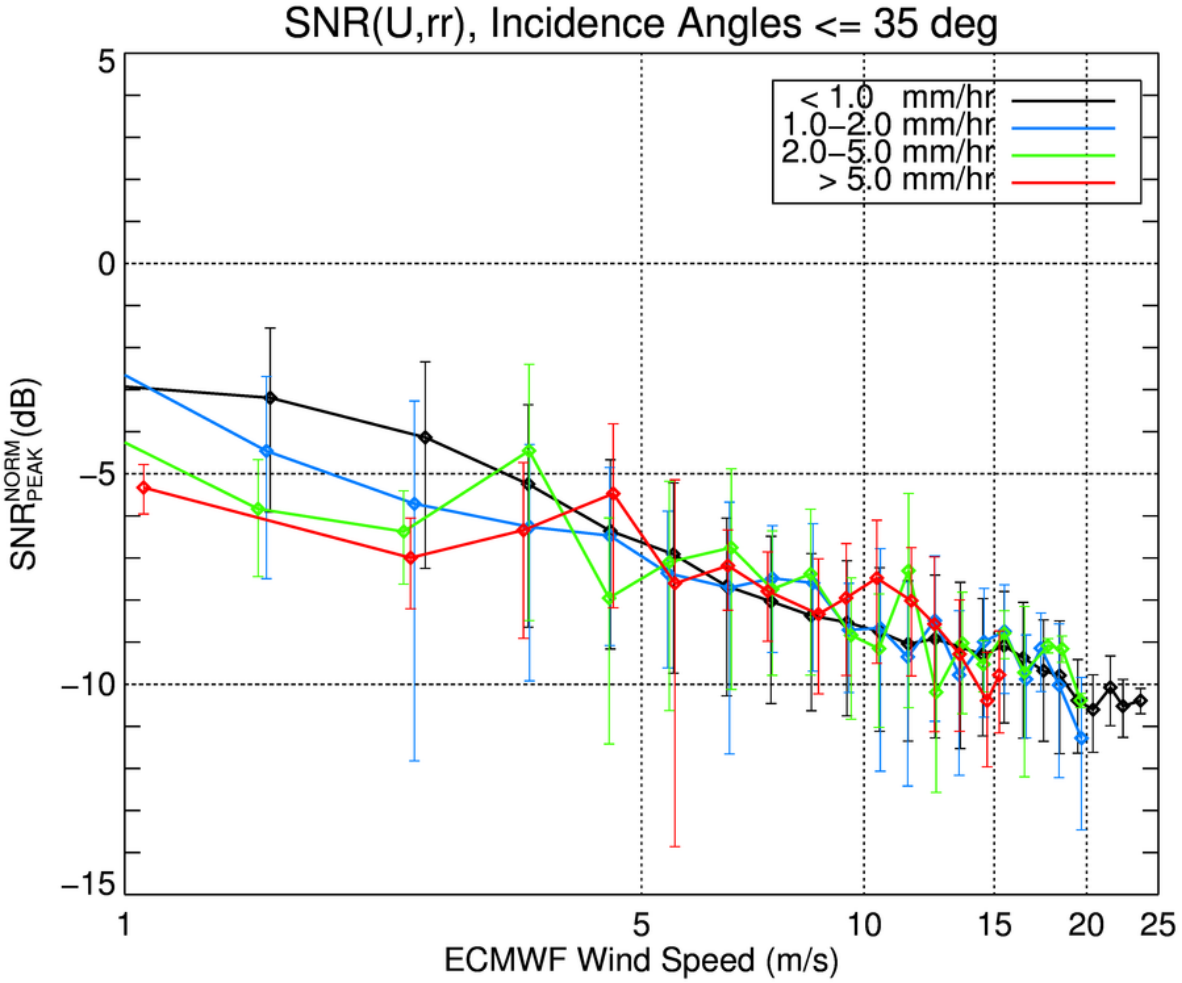

Fig. 23. The SGR-ReSI SNR_{PEAK}^{NORM} as a function of ECMWF wind speed with average rain rate from collocated GMI measurements as parameters.

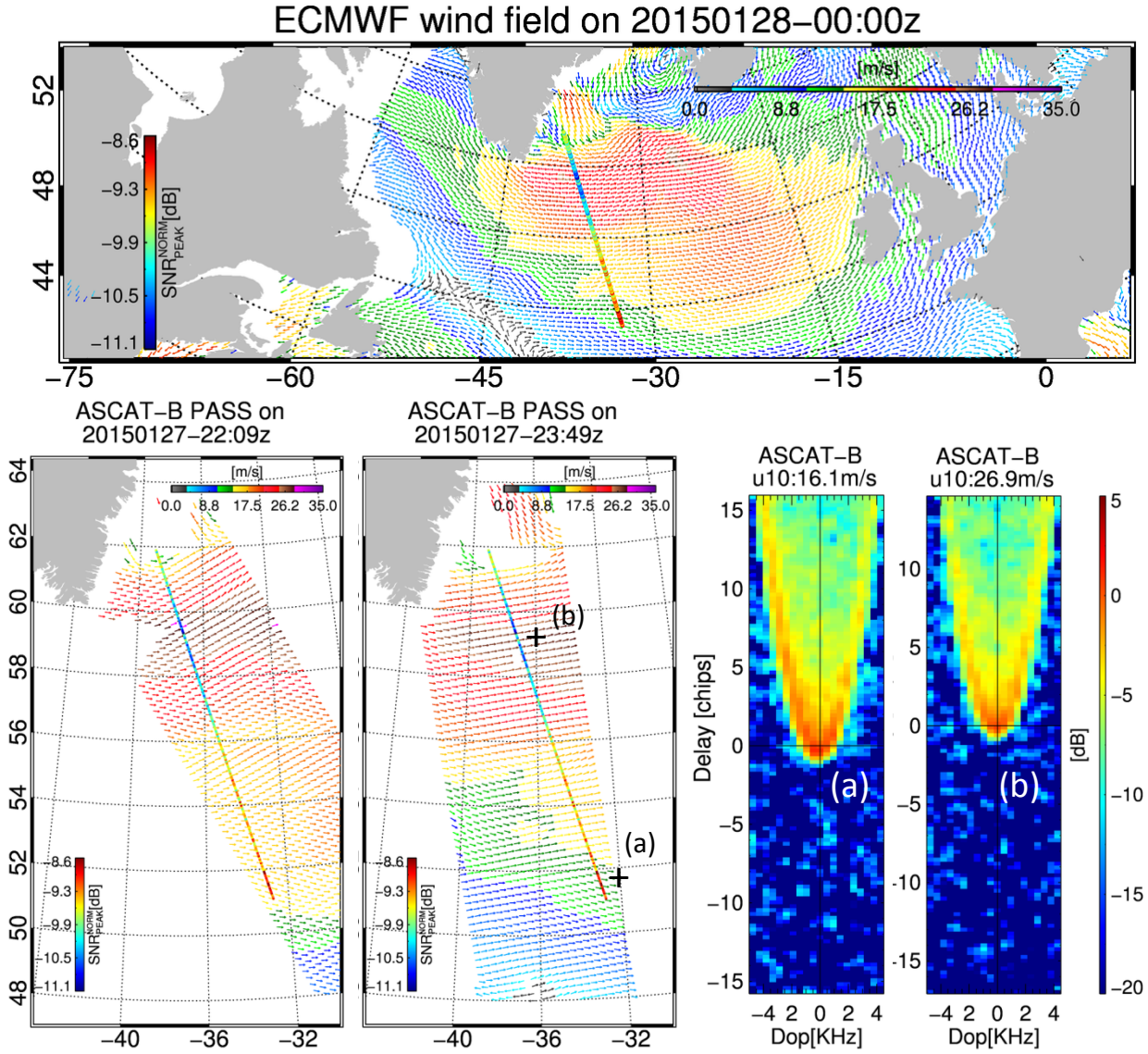

Fig. 24. 22:09Z and 23:50Z ASCAT passes, and corresponding ECMWF model run valid at 00:00Z on January 27, 2015, over an extratropical cyclone system. The colored line transecting the ASCAT-B swaths represents the TDS - 1 SGR ReSi pass at 23:16Z. The varying color along the transect denotes the SNR_{PEAK}^{NORM} values. The DDM's from two specular points (depicted with plus symbols over the ASCAT-B swath) correspond to 16 m/s winds (a) and 27 m/s winds (b), respectively.

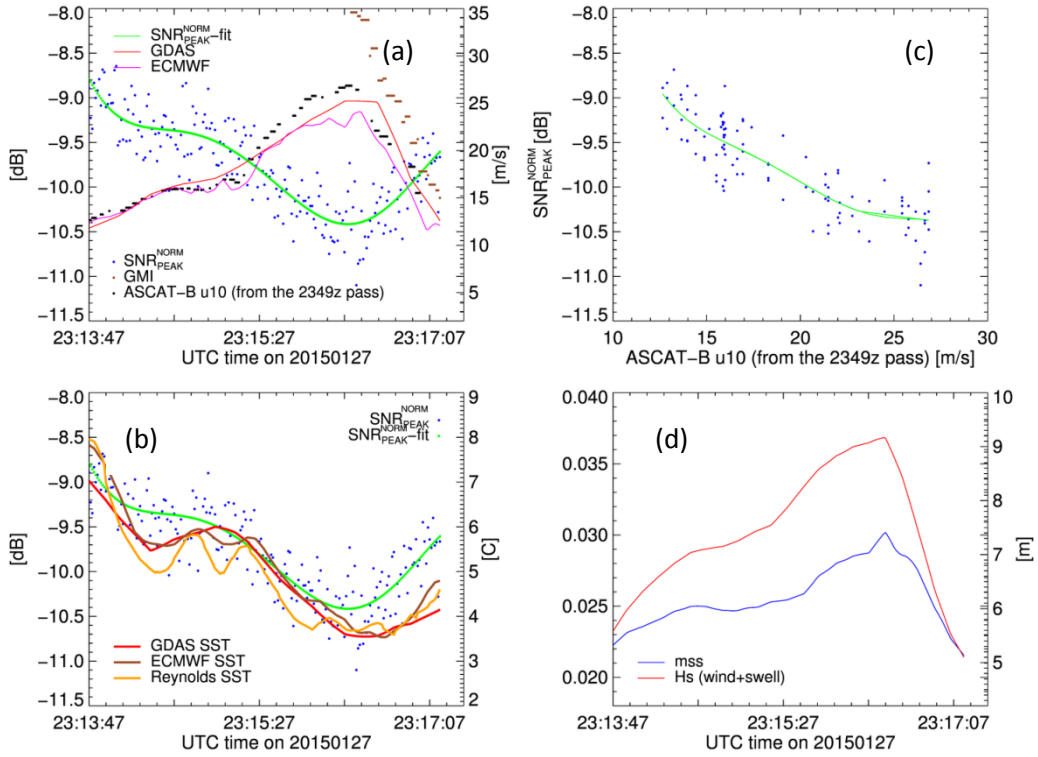

Fig. 25. Timeseries of ASCAT-B, ECMWF, GDAS, and GMI wind speeds (a), and ECMWF, GDAS and Reynolds SST (b) along the TDS-1 SGR-ReSI track. Plot (c) shows corresponding SNR_{PEAK}^{NORM} variations (blue dots) as a function of ASCAT-B wind speed. Plot (d) shows the corresponding MSS and H_S values along the track

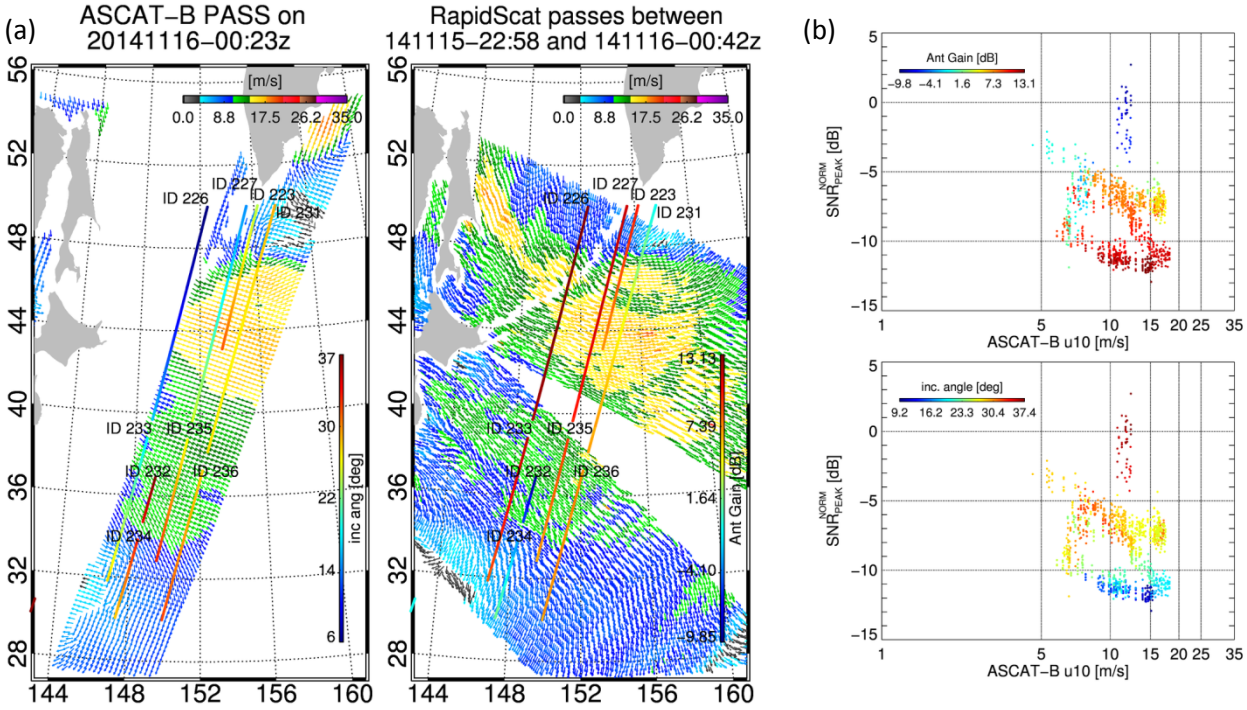

Fig. 26. (a) Multiple TDS-1 SGR-ReSi transects over a changing wind field that correspond with an ASCAT-B pass at 00:23Z on November 16, 2014, and two RapidScat passes at 22:58Z on November 15, 2014, and 00:43Z on November 16, 2014. Each transect represents a series of sea surface reflected signals from a given GPS satellite sensed by the SGR ReSI receiver as identified with different track ID. (b) Measured SNR_{PEAK}^{NORM} for each track as a function of ASCAT-B retrieved wind speed and antenna gain (top) and incidence angle (bottom) as parameters.

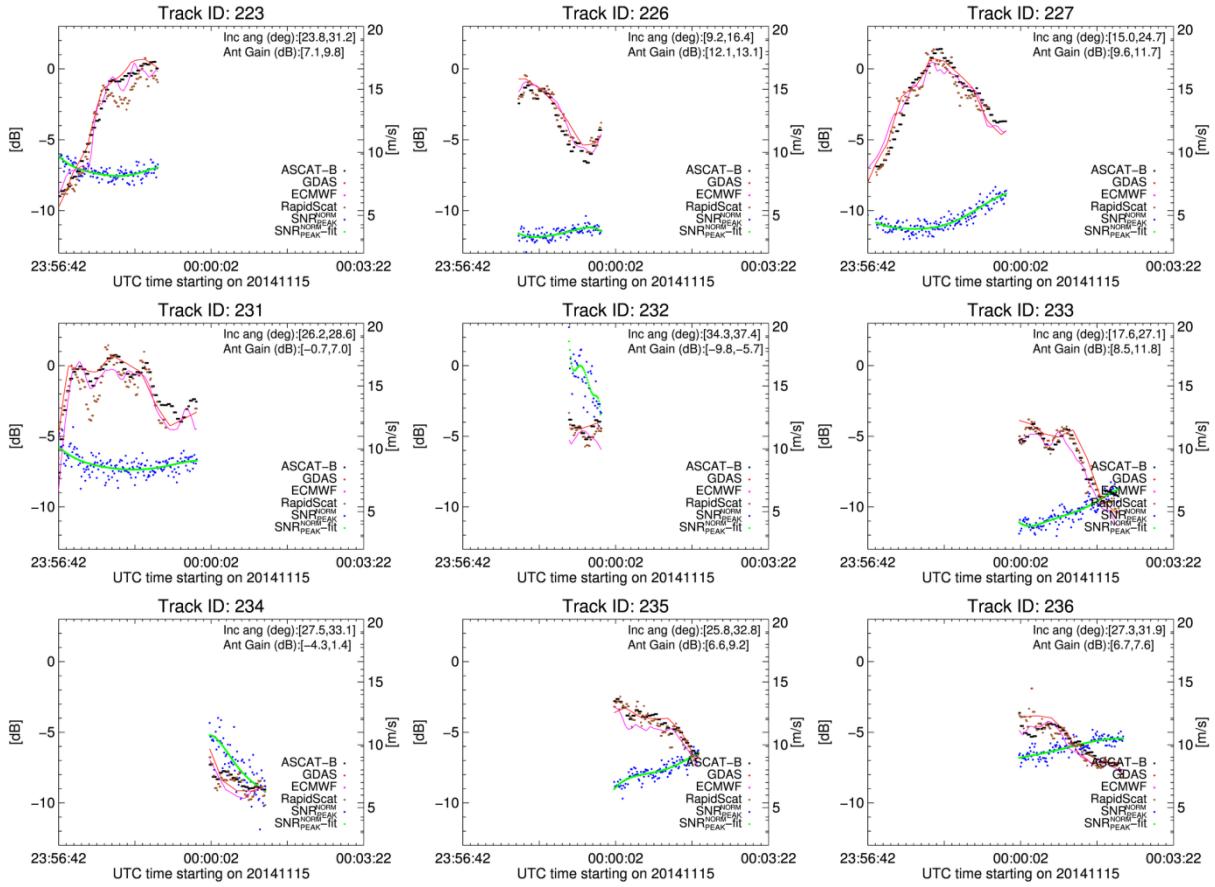

Fig. 27. The time series of measured SNR_{PEAK}^{NORM} along different TDS-1 SGR-ReSi tracks depicted by different ID numbers, and the corresponding time series of collocated ASCAT-B retrieved wind speeds

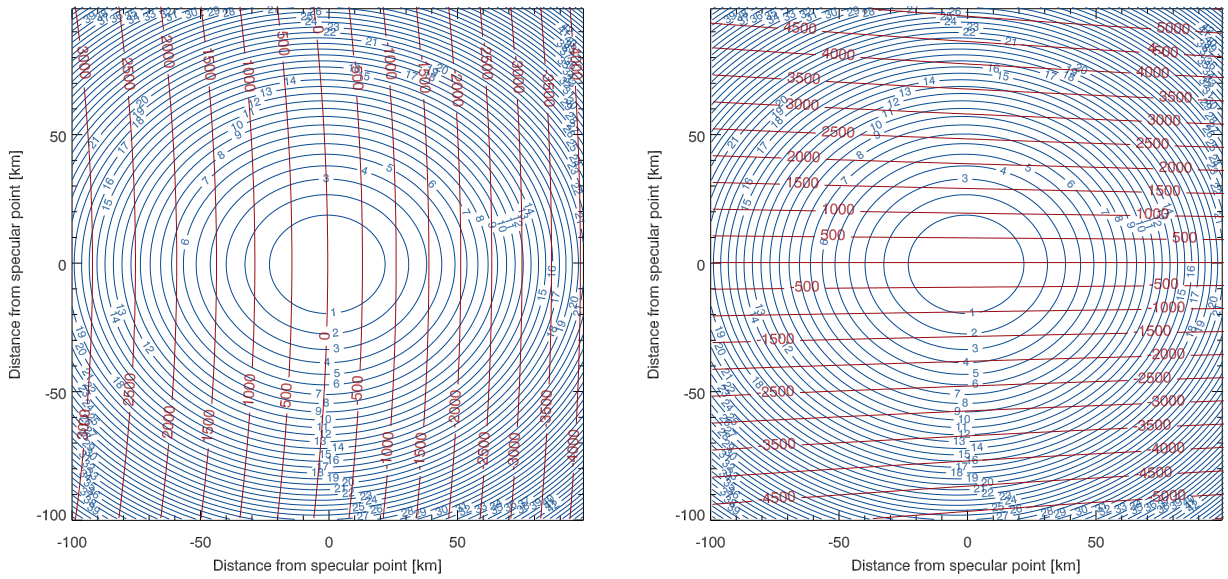

(a) (b)

Fig. A1. Iso-delay and iso-Doppler lines for (a) parallel and (b) perpendicular velocities with respect to the incidence plane. The iso-delay contours are labeled as delay chips and iso-Doppler lines are labeled in Hz, both are with respect to the specular point.

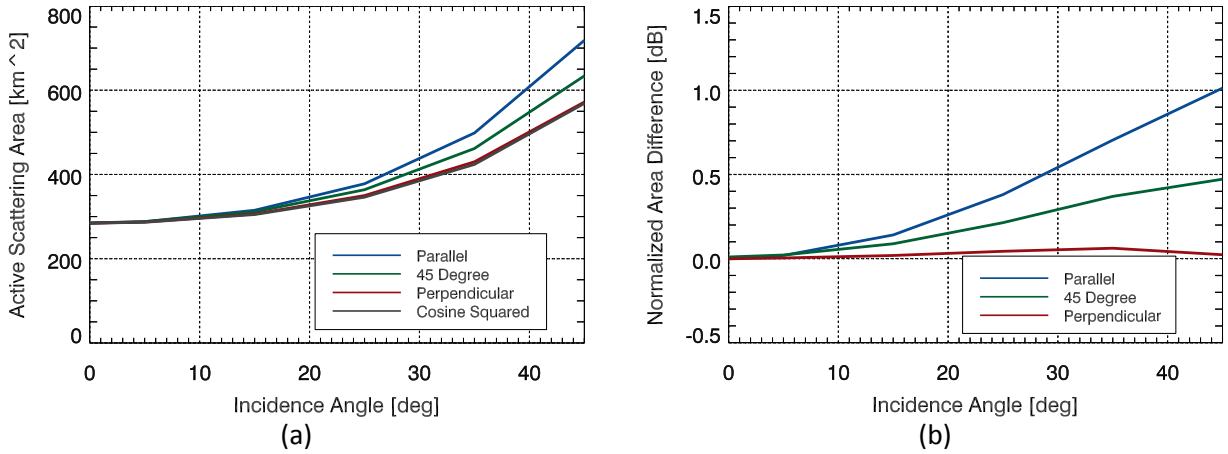

Fig. A2. Active scattering areas as a function of incidence angle for a TDS velocity parallel, perpendicular, and at 45° with respect to the incidence plane where (a) is un-normalized, and (b) is normalized with respect to $1/\cos^2$ curve.

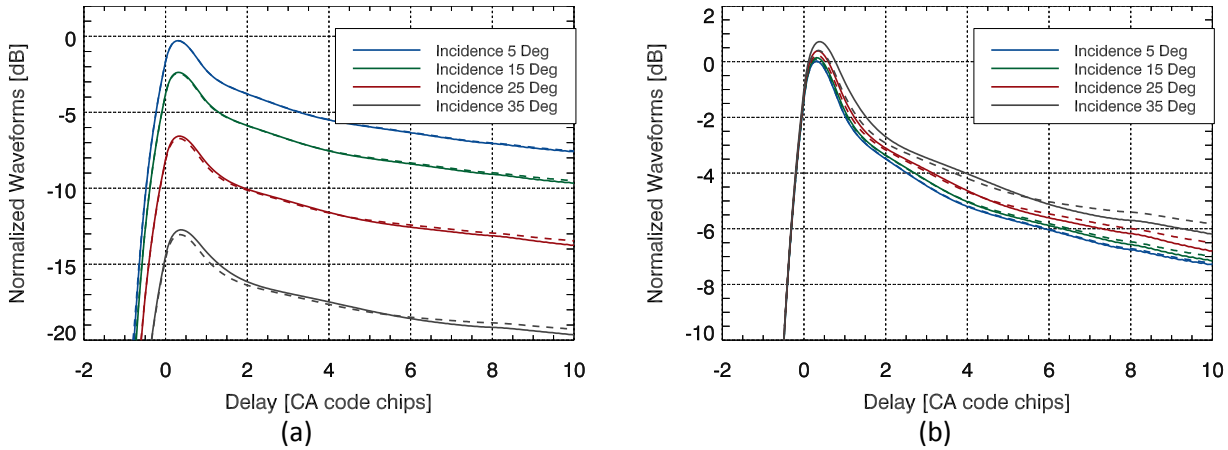

Fig. A3. Numerically computed waveforms. (a) Normalized by the nadir peak power, and (b) normalized by *CF*.